AGU ADVANCING EARTH AND SPACE SCIENCES

JGR Planets

RESEARCH ARTICLE

10.1029/2026JE009697

Martian Proton Albedo as Signature of Near-Surface Water

Jan Leo Löwe[1], **Robert F. Wimmer-Schweingruber**[1], **Salman Khaksari**[1], **Sven Löffler**[1], **Sergey Nikiforov**[2,3], **Maya Djachkova**[2], **Jingnan Guo**[4], **Gabin Charpentier**[5,6], **Bent Ehresmann**[7], **Donald M. Hassler**[7], **Daniel Matthiä**[8], **Thomas Berger**[8], **Günther Reitz**[8], and **Cary Zeitlin**[9]

[1]Institute of Experimental and Applied Physics, Christian-Albrechts-University, Kiel, Germany, [2]Space Research Institute of the Russian Academy of Sciences (IKI), Moscow, Russia, [3]Center for Astrophysics and Space Science (CASS), New York University Abu Dhabi, Abu Dhabi, UAE, [4]Deep Space Exploration Laboratory/School of Earth and Space Sciences, University of Science and Technology of China, Hefei, PR China, [5]Centre National d'Études Spatiales (CNES), Toulouse, France, [6]TRAD Tests & Radiations, Labège, France, [7]Planetary Science Division, Southwest Research Institute, Boulder, CO, USA, [8]German Aerospace Center (DLR), Institute of Aerospace Medicine, Cologne, Germany, [9]Leidos Corporation, Houston, TX, USA

Key Points:

- We present a novel investigation of Martian near-surface water using albedo protons
- Small variations in the soil's water budget of 2%–7% could not be measured by Mars science laboratory/radiation assessment detector to date
- Simulations suggest that larger near-surface water reservoirs could be identified with sufficient measurement time

Supporting Information:

Supporting Information may be found in the online version of this article.

Correspondence to:

J. L. Löwe and R. F. Wimmer-Schweingruber,
loewe@physik.uni-kiel.de;
wimmer@physik.uni-kiel.de

Citation:

Löwe, J. L., Wimmer-Schweingruber, R. F., Khaksari, S., Löffler, S., Nikiforov, S., Djachkova, M., et al. (2026). Martian proton albedo as signature of near-surface water. *Journal of Geophysical Research: Planets*, *131*, e2026JE009697. https://doi.org/10.1029/2026JE009697

Received 30 JAN 2026
Accepted 5 MAY 2026

Author Contributions:

Conceptualization: Jan Leo Löwe, Robert F. Wimmer-Schweingruber
Formal analysis: Jan Leo Löwe
Investigation: Jan Leo Löwe
Methodology: Jan Leo Löwe, Robert F. Wimmer-Schweingruber, Salman Khaksari
Resources: Sergey Nikiforov
Supervision: Robert F. Wimmer-Schweingruber
Writing – original draft: Jan Leo Löwe
Writing – review & editing: Salman Khaksari, Sven Löffler, Sergey Nikiforov, Jingnan Guo, Gabin Charpentier, Daniel Matthiä

Abstract

Understanding the Martian soil water budget is crucial not only for in situ resource utilization in future human missions to Mars, but also for reconstructing the geological and climatic history of the planet, as well as to assess the potential of ancient or even present microbial life. Here, we present a methodology to study near-surface water using albedo protons, based on measurements from the Radiation Assessment Detector (RAD) onboard the Mars Science Laboratory (MSL). With this approach, water can be investigated beneath dust layers at approximately 1–6 cm, representing a new observational depth range compared to existing methods. In combination with data from the Dynamic Albedo of Neutrons (DAN) experiment, also part of MSL, we show that MSL/RAD has so far been unable to resolve small variations in regolith water of 2%–7%. However, supporting simulations suggest that larger water reservoirs, such as those at higher latitudes or locally near the equator, may be detected by MSL/RAD with measurement times of approximately two to 3 months. We demonstrate that a future Mars detector, specifically redesigned to measure albedo protons, could detect changes in near-surface water content of about 20% within roughly 6–16 days, and variations exceeding 40% within only a few days, with statistical significance. We therefore propose including albedo proton measurements in future missions to Mars or other extraterrestrial bodies, as they represent a promising complement to existing methods for probing near-surface water.

Plain Language Summary

Studying water on Mars is essential for understanding the planet's history, assessing its habitability and microbial activity, as well as supporting future crewed missions. Sample collection methods are the most promising but require significant effort. Therefore, we focus on detecting water signatures in upward-directed radiation produced by interactions between Martian surface radiation and the soil. Upward-directed neutrons have been extensively studied, but upward-directed protons could also be promising, as fewer protons are expected in hydrated soil compared to dry soil (Schwadron et al., 2016, https://doi.org/10.1016/j.icarus.2015.12.003). That is why we developed a procedure to measure upward-directed protons with the Radiation Assessment Detector (RAD) onboard Mars Science Laboratory (MSL) and link them to the soil's water content determined by the Dynamic Albedo of Neutrons (DAN) experiment. Although our measurements do not allow conclusions about small variations in soil water content so far, simulations suggest that larger near-surface water reservoirs could likely be identified with MSL/RAD with sufficient measurement time. A detector specifically designed to measure albedo protons can resolve variations in soil water content within significantly shorter measurement times, making it a promising complement to existing methods for probing water in soil in future Mars missions.

1. Motivation and Introduction

Geological features, such as apparent river scars, deltas, and possible shorelines (Carr, 1986; Carr & Head, 2003; Di Achille & Hynek, 2010; Parker et al., 1989), together with the discovery of coral-shaped rocks (Armstrong, 2022), indicate that Mars likely hosted a warm, wet environment over 3 billion years ago (Jakosky & Phillips, 2001; Ramirez et al., 2020). However, today Mars appears to be a cold, arid, and inhospitable desert planet, implying that most of its water reservoir has vanished over time. The driving mechanism of Martian water loss is commonly attributed to sputtering, reported for example, by NASA's "Mars Atmosphere and Volatile Evolution" (MAVEN) mission (Jakosky et al., 2015), where the absence of a global magnetic field allows the solar wind to penetrate deeply into the unprotected atmosphere, physically knocking atoms into space (Jakosky et al., 2018). Because liquid water is not stable on the Martian surface and water vapor continuously dissociates in the atmosphere, hydrogen can also escape into space (Chaffin et al., 2021; Donahue, 1995; Villanueva et al., 2015; Webster et al., 2013). Recent studies on the atmospheric deuterium-to-hydrogen ratio (Scheller et al., 2021), however, indicate that a substantial fraction of Mars' initial water might not have escaped into space but may instead have been incorporated into minerals in the planet's crust, later becoming buried.

Studying Mars' subsurface water content is crucial for assessing the possibility of microbial life on ancient Mars or even its potential persistence to the present day (Atri et al., 2025; Dartnell et al., 2007; Hurowitz et al., 2025). Additionally, it has important implications for future Mars colonization, both for in situ resource utilization and for providing humans with indirect radiation shielding (G. A. Morgan et al., 2021; Röstel et al., 2020). Understanding the abundance and distribution of underground water in potential Mars landing zones is also paramount for future crewed or robotic missions for two reasons. First, hidden subsurface ice could affect surface roughness and traction, endangering a safe landing (G. A. Morgan et al., 2021). Second, landing sites must comply with the COSPAR planetary protection policy (Olsson-Francis et al., 2023) to avoid inadvertently contaminating potential Martian life in water with terrestrial organisms (Rummel et al., 2014). Finally, by understanding the underground and surface water budget on Mars, it may be possible to reconstruct its history, including past climate conditions, the development of geological landforms, and past and present global water cycles (Mellon & Jakosky, 1995; Steele et al., 2017).

Therefore, the subsurface water budget on Mars has been studied intensively for over half a century. Near the equator, within the ±45° latitude range, the abundance of subsurface water is generally estimated based on measurements from the "Mars Odyssey Neutron Spectrometer" (MONS; Mesick et al., 2020) to be between 2 wt.% and 10 wt.% (Feldman et al., 2004). Similarly, the "Observatoire pour la Minéralogie, l'Eau, les Glaces, et l'Activité" (OMEGA) instrument aboard Mars Express detected water stored in hydrated silicates, with a spatial average of 5.2 ± 2.8 wt.% over the surface between −60° and 60° latitude (Riu et al., 2023). Measurements from the "Dynamic Albedo of Neutrons" (DAN; Litvak et al., 2008) instrument, part of the "Mars Science Laboratory" (MSL; Grotzinger et al., 2012), support these findings: In Gale Crater (latitude: −5.4°, longitude: 137.9°), subsurface water is estimated to range from almost zero up to (6.1 ± 0.7) wt.% (Nikiforov et al., 2020; Tate et al., 2015). Soil analyses from both Viking missions (Klein, 1979) Viking 1 (latitude: 22.3°, longitude: −48.2°) and Viking 2 (latitude: 47.7°, longitude: 134.1°) yielded roughly 1–3 wt.% water (Anderson & Tice, 1979). Similarly, Mars Pathfinder (Golombek et al., 1997) alpha proton X-ray spectrometer data (latitude: 19.3°, longitude: 33.6°) indicate the average water mass fraction for soil ranging up to 1.7% and for rocks ranging up to (4.3 ± 1.3)% (Foley et al., 2003). However, MONS also identified small regions at low and mid latitudes with elevated underground water content, including ∼10 wt.% on the flanks of Tharsis Montes (latitude:−20°–20°, longitude: 230°–260°) and >40 wt.% at the Medusae Fossae Formation (latitude: −15°–15°, longitude:130°–240°) (Wilson et al., 2018). The western lobes of the Medusae Fossae Formation, including Aeolis, Zephyria, and Lucus Planum, also contain WEH contents exceeding 10 wt.% (Wilson et al., 2018). Results from Pathare et al. (2018) further indicate low-latitude water reservoirs exceeding 15 wt.% in several regions, including Arabia Terra (latitude: −18.07°–45.36°, longitude: −29.69°–49.44°). In addition to Arabia Terra and the Medusae Fossae Formation, Malakhov et al. (2022) identified another localized water-rich region with approximately 20 wt.% WEH in Arcadia Planitia (latitude: 33.9°–64.2°, longitude: 165.9°–210.4°). Poleward of approximately ±60° latitude, analyses of MONS data reveal large reservoirs of subsurface water ranging from 25 wt.% to nearly 100 wt.% (Boynton et al., 2002; Feldman et al., 2002, 2004; Mitrofanov et al., 2004; Wilson et al., 2018), depending on location and model. These results are interpreted as water–ice layers within the uppermost meter of Martian soils, with layers at high northern latitudes located near the surface, whereas in the south they are overlain by a desiccated, relatively thick soil layer (10–20 cm) (Litvak et al., 2006). In these latitude regions, the Phoenix lander (latitude: 68.21°, longitude: 234.25°) scooped samples, in which Smith et al. (2009) also found a layer of ice at depths of 5–15 cm. At Planum Boreum itself, the northern pole, "Mars Reconnaissance Orbiter Shallow Radar" (MRO/SHARAD; Seu et al., 2004; Seu et al., 2007) detected alternating subsurface layers of ice and sand, with water volume fractions estimated at approximately 62%–88%. These results are interpreted as remnants of the former ice caps, protected from complete sublimation during warmer periods by aeolian sand and/or sublimation residues (Nerozzi & Holt, 2019). Ojha et al. (2019) analyzed gravity and topography data, also suggesting that the northern polar cap may contain 55 ± 25% water ice. At Planum Australe, the Martian south pole, the "Mars Advanced Radar for Subsurface and Ionosphere Sounding" (MARSIS) on the Mars Express spacecraft (Picardi et al., 2005) has unveiled multiple subglacial bodies of liquid water beneath layers of solid ice and dust (Lauro et al., 2021; Orosei et al., 2018). The exposed surface H_2O ice is also present in Planum Australe, as observed with the Mars Odyssey Thermal Emission Imaging System (THEMIS; Christensen et al., 2004, cf. Titus et al., 2003). This exposed surface ice varies seasonally due to condensation and sublimation, as indicated by measurements from the Emirates Mars Infrared Spectrometer aboard the Emirates Mars Mission (EMM; Amiri et al., 2022), affecting surface frost even down to equatorial latitudes (Stcherbinine et al., 2023). A comprehensive overview of the approaches and results in the search for water on Mars can be found in Nazari-Sharabian et al. (2020).

In this paper, we present a novel investigation of Martian subsurface water based on protons originating from the soil. This technique has already been applied and studied on the Moon (see e.g., Schwadron et al., 2016; Wilson et al., 2012; Xu et al., 2022), and here we transfer the concept to Martian conditions. The proton-based approach could provide a new window for studying the regolith water budget on Mars, complementary to existing techniques. It is potentially sensitive to different depths of the Martian soil and, if successfully applied, could serve to verify or challenge existing findings.

The paper is structured as follows: First, we describe the radiation environment on Mars in Section 2, with a particular focus on the interaction of radiation with the Martian soil depending on its water content. Next, in Section 3, we introduce the instruments used and the necessary datasets for our study. Since our measurements are supported by model calculations, Section 4 describes the simulation tool and the setup employed. Section 5 outlines our methodology for probing near-surface water using protons, followed by the measurement results in Section 6 and the simulation results in Section 7. Both are discussed and limitations are addressed in Section 8. Finally, we summarize and conclude our findings in Section 9.

2. The Radiation Environment on the Surface of Mars

In addition to sporadically occurring Solar Energetic Particle (SEP) events, the radiation environment at the surface of Mars is primarily dominated by Galactic Cosmic Rays (GCRs), which originate outside the solar system, presumably from supernovae and neutron star mergers (Baade & Zwicky, 1934; Butt et al., 2002; Ginzburg & Syrovatskii, 1964; Takami et al., 2014). GCRs consist predominantly of protons (∼87%), but also include alpha particles (∼12%), electrons (∼1%), and traces of fully ionized heavier nuclei (∼1%–2%). Their energies range from below 1 MeV/nuc to a maximum intensity around 300–500 MeV/nuc, extending up to hundreds of TeV/nuc, essentially following a power-law distribution (Engelmann et al., 1990; Mewaldt, 1994; Simpson, 1983; Wiebel-Sooth et al., 1998).

Within the solar system, variations in GCR flux and energy spectrum are modulated by the Sun's varying activity, including periodic variations associated with the ∼11-year solar cycle and the ∼27-day heliospheric rotation (Cane, 2000; Jokipii & Thomas, 1981; Potgieter, 2013; Usoskin, 2023). Non-relativistic GCR protons below 100–200 MeV are most responsive to changes in solar conditions, while higher-energy protons exhibit progressively smaller effects. At energies above 30–50 GeV, the effect of solar modulation on GCRs can be considered negligible (Heber & Potgieter, 2006; Strauss & Potgieter, 2014; Vos & Potgieter, 2015). Upon reaching Mars, GCRs can penetrate deep into the Martian atmosphere because Mars lacks a global magnetic field. Given the thin atmosphere of Mars, with an average surface density of $\rho_{\text{Mars}} \sim 0.016\ \text{kg/m}^3$ (∼1% of Earth's) (Alexander, 2001), GCR protons with energies above approximately 140–190 MeV can reach the surface directly (Guo, Wimmer-Schweingruber, et al., 2019). Heavy ions have even higher MeV/n atmospheric cutoff thresholds (Guo, Slaba, et al., 2017; Guo, Wimmer-Schweingruber, et al., 2019). GCRs without sufficient energy to reach the surface can still produce secondary particles through nuclear reactions such as spallation and fragmentation, which may themselves reach the surface. Consequently, protons and heavier nuclei dominate the surface radiation environment above a few hundred MeV, whereas at lower energies, secondary neutral particles (neutrons and γ-rays) prevail (Ehresmann et al., 2014; Gonçalves et al., 2022; Matthiä & Berger, 2017). However, both the cutoff energy and the production of atmospheric secondaries are closely linked to the variability of the Martian atmosphere, which undergoes diurnal and seasonal changes. Diurnal pressure fluctuations are caused by strong thermal tides, excited by direct solar heating of the dayside (decrease in atmospheric surface pressure) and strong infrared cooling on the nightside (increase in atmospheric surface pressure) (S. C. R. Rafkin et al., 2014). Seasonal

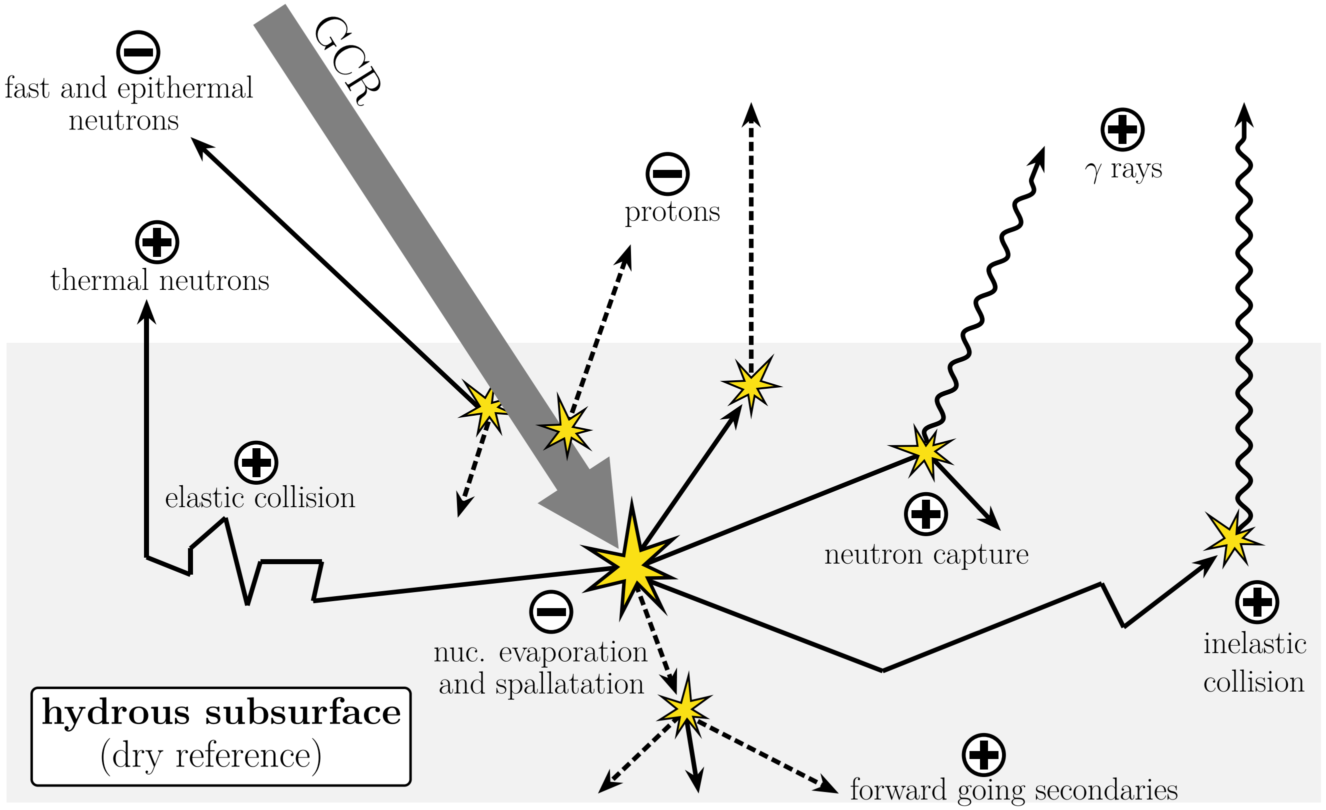

Figure 1. Simplified schematic of a Galactic Cosmic Ray (or a particle produced in the atmosphere) reaching the surface of Mars, interacting with the nuclei of the regolith, generating particles including neutrons ↑, protons ⇡, and gamma rays ↝. The number and energy of albedo particles depend on the physical processes in the soil, which are influenced by the hydrogen content in the regolith. Processes that occur more frequently or produce more particles in a hydrous subsurface compared to a dry subsurface are indicated with ⊕, whereas the opposite is indicated with ⊖. Each interaction occurring in the subsurface is represented by a flash point ✷ in the diagram. Other cascade interactions that occur in the atmosphere are not shown.

variations in surface pressure are driven by the sublimation and deposition cycles of the CO_2 polar ice caps (Guo, Slaba, et al., 2017).

Upon reaching the Martian surface, both primary GCRs and atmospheric secondaries can interact with the regolith, penetrating to depths of up to ~1 m (Jun et al., 2013; Röstel et al., 2020). They collide with nuclei in the soil, either scattering elastically or generating showers of energetic particles through nuclear evaporation, predominantly neutrons and protons (see central collision in Figure 1). Upward-directed particles that re-emerge from the soil into the atmosphere are referred to as "albedo" particles. Neutrons may either escape directly as fast neutrons (1–20 MeV) without undergoing significant interactions in the soil, or as epithermal (0.025–0.4 eV) and thermal (~0.025 eV) neutrons after being moderated through elastic collisions with other nuclei in the regolith. The majority of neutrons escaping the surface originate from depths of ~60 cm (Jun et al., 2013). Neutrons that do not escape as albedo particles gradually lose energy until they approach thermal equilibrium with the surrounding material. They are eventually absorbed through neutron capture, which produces gamma rays. Additional gamma rays can be generated by inelastic collisions of fast neutrons with soil nuclei (Martinez Sierra et al., 2023; Prettyman et al., 2006), potentially contributing to the albedo gamma-ray flux. Protons, either produced in nuclear interactions within the soil or by simple backscattering of incident GCR protons, can also emerge as albedo particles. Unlike neutrons and gammas, protons continuously lose energy through strong ionization in addition to elastic and inelastic scattering due to their electric charge. Consequently, the production depth of albedo protons is assumed to be much shallower than that of neutrons and gammas, presumably only a few centimeters (Schwadron et al., 2018).

The hydrogen content in the regolith can significantly affect the physical processes occurring in the subsurface and, consequently, the production of albedo particles. A higher subsurface water content reduces nuclear evaporation, as there is no excited residual nucleus after a collision with a hydrogen nucleus, and therefore no de-excitation (Schwadron et al., 2016). Hydrogen is also lighter than other atoms in the soil, reducing the average Z of hydrated material compared to dry regolith. The result is more forward-directed interactions and reduced backscattering (Schwadron et al., 2016). Another consequence is that elastic and inelastic collisions are more frequent in hydrated material, as both depend on the target nucleus mass, with more energy transferred to lighter nuclei. Consequently, hydrogen is highly effective at causing incident particles to lose energy, leading to stronger modulation to lower energies and an increased likelihood of particles trapping within the regolith. For different albedo particle species, this implies that a higher soil water content is expected to:

1. Reduce the yield of fast and epithermal albedo neutrons, while increasing thermal neutrons, as more elastic collisions occur in the soil and neutrons are more frequently moderated from fast to epithermal to thermal energies, respectively (Drake et al., 1988; Kim & Kim, 2026; Tate et al., 2019).
2. Increase albedo gamma rays, since neutron capture in the soil becomes more probable and more inelastic collisions can occur (Boynton et al., 2002; Prettyman et al., 2006).
3. Reduce the albedo proton yield, because nuclear evaporation is suppressed and more incident energy goes into forward-directed interaction products (Schwadron et al., 2016).

The GCR–soil interaction, contrasting dry and hydrated regolith, is schematically depicted in Figure 1. Subsurface water detection via albedo neutrons and gamma rays is well established (e.g., MSL/DAN, Mars Odyssey GRS (Boynton et al., 2004), MONS). In contrast, albedo-proton-based studies of Martian subsurface water remain unexplored and are addressed in this paper. Although albedo particle measurements can apparently provide information on soil water content, they do not reveal whether hydrogen is present as liquid water, ice, or within hydrated minerals. Therefore, in the following, we use the commonly adopted terminology in the literature, "Water-Equivalent Hydrogen" (WEH) content. Nevertheless, since hydrogen is generally assumed to be primarily associated with water molecules, its detection is typically interpreted as an indication of the presence of water (Malakhov et al., 2022; Mitrofanov et al., 2022).

3. Instruments and Data Sets

In this study, we use measurements from two instruments located on the surface of Mars, both onboard MSL's Curiosity rover. The first, the Radiation Assessment Detector (RAD; Hassler et al., 2012), is currently the only Martian detector capable of resolving the directionality of protons. Its key advantage lies in its surface location: unlike instruments orbiting Mars, MSL/RAD can detect albedo protons coming from the soil, which are otherwise shielded by the Martian atmosphere. Based on these data, we develop a method to identify albedo protons and link them to near-surface WEH content. The second instrument, MSL/DAN, is specifically dedicated to determining the water content in the Martian regolith. Since MSL/DAN is mounted on the same rover as MSL/RAD, it provides the ideal reference to validate or falsify our findings. It is worthwhile to note that a drilling campaign, as documented by Abbey et al. (2019), could in principle also serve as a cross-check of the regolith water content. However, because the data points are spatially irregular and sampling of wet or sticky material is intentionally avoided due to its potential to clog the system (Abbey et al., 2019), the MSL/DAN data provide a more suitable basis for comparison.

3.1. The Radiation Assessment Detector

MSL/RAD is mounted on top of the Curiosity rover, and its configuration is schematically shown in Figure 2. It consists of three silicon diodes (A, B, and C) at the top of the detector stack, followed by a thallium-doped cesium iodide scintillator (D) and a plastic scintillator (E). The inner segment of detector A is designated A2, while the outer segment is A1. Scintillators D and E are surrounded laterally by an additional plastic scintillator (F1) and are enclosed at the bottom by another plastic scintillator (F2), both serving as anticoincidence detectors. A detailed description of MSL/RAD is given in (Hassler et al., 2012).

In addition to the primary dosimetric quantities (cf. Guo et al., 2015; Guo, Zeitlin, et al., 2021) and neutral particles (cf. Guo, Zeitlin, et al., 2017; Köhler et al., 2014), MSL/RAD also measures charged particles. A coincidence trigger on detectors A and B is used to define the acceptance angle for incoming charged particles: the inner field of view (FOV) is $A2 \times B = 36°$ and the combined inner and outer FOV is $(A1 + A2) \times B = A \times B = 60°$ (Zeitlin et al., 2013). The former results in a geometry factor of $G_{A2 \times B} = 0.17\ \mathrm{cm}^2$ sr, while the latter yields a geometry

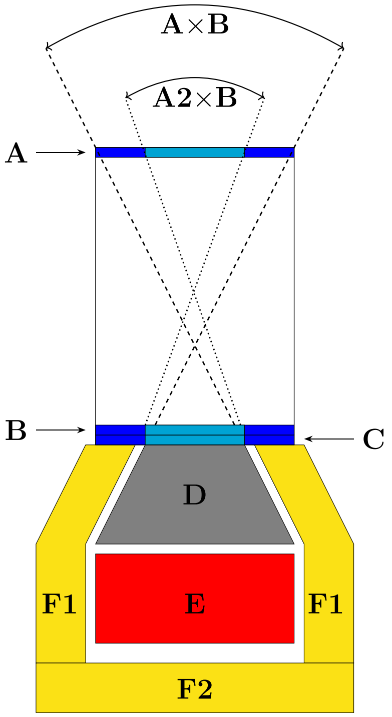

Figure 2. Schematic of Mars Science Laboratory/Radiation Assessment Detector, adopted from Löwe et al. (2025). The detector stack consists of three silicon detectors (A, B, and C) followed by two plastic scintillators (D and E). Two additional plastic scintillators (F1 and F2) serve as (anti)coincidence detectors. The segmentation of detector A into A1 and A2 defines two fields of view: A2 × B = 36° and A × B = 60°.

factor of $G_{(\mathrm{A1}+\mathrm{A2})\times \mathrm{B}} = 0.90\ \mathrm{cm}^2\ \mathrm{sr}$ (Hassler et al., 2012). The inner FOV not only ensures that all charged particles cannot exit the detector stack from the sides, but also allows MSL/RAD to distinguish between stopping and penetrating charged particles. The maximum energy that a stopping ion coming to rest in detectors B, C, D, or E can deposit ranges from approximately 10–100 MeV for protons up to $\sim 400\,\frac{\mathrm{MeV}}{\mathrm{nuc}}$ for iron ions. Higher-energy ions penetrate the detector stack. For protons, this occurs at primary energies of approximately $E_{\mathrm{prim}} = 100$ MeV. Each penetrating particle event is flagged by requiring an energy deposit of $\geqslant$100 keV in each silicon detector A2, B, and C, $\geqslant$1 MeV in the plastic scintillators D and E, and $\geqslant$1 MeV in the anticoincidence detector F2. In addition, MSL/RAD can resolve the direction of penetrating particles with primary energies of $E_{\mathrm{prim}} = 100\text{–}200\,\frac{\mathrm{MeV}}{\mathrm{nuc}}$ (corresponding to an energy deposition in MSL/RAD of $\sim 45 - 100\,\frac{\mathrm{MeV}}{\mathrm{nuc}}$), that is, whether they enter the detector stack from above or below (Appel et al., 2018).

MSL/RAD has been monitoring the radiation environment on the surface of Mars since landing on 6 August 2012. Over time, instrument calibration has occasionally changed (Zeitlin et al., 2016), with the last major adjustment occurring on 9 June 2017. Since calibration prior to this date was changed more frequently, we exclude this earlier period to ensure a consistent analysis. After 2017 June 9, calibration was modified only once more, on 26 June 2018, which we carefully account for in our analysis.

3.2. The Dynamic Albedo of Neutrons Experiment

The core components of the MSL/DAN instrument are two high-pressure ^{3}He proportional counters. The first counter is unshielded and detects neutrons with energies up to ~1 keV. The second counter is wrapped in cadmium, which strongly absorbs neutrons with energies up to ~0.4 eV and therefore detects neutrons in the range ~0.4 eV to ~1 keV (Jun et al., 2013; Tate et al., 2019). Thus, MSL/DAN measures thermal and epithermal neutrons continuously in the so-called "passive mode," originating from the interactions of GCRs and secondary atmospheric particles with the Martian soil. As described in Section 2, a higher hydrogen content in the soil leads to a relative decrease in epithermal neutrons and an increase in thermal neutrons. By measuring this ratio, MSL/DAN can infer the WEH content of the Martian soil down to depths of ~50–60 cm (Dibb et al., 2024; Jun et al., 2013).

In addition, MSL/DAN is equipped with a neutron generator that produces 14.1 MeV neutrons. In this "active mode," MSL/DAN emits short pulses of about 2–3 microseconds of these high-energy neutrons toward the soil, and the ^{3}He counters record the time profile of thermal and epithermal neutrons returning from lateral distances of up to about 1–1.5 m and depths of up to roughly 60 cm in the subsurface (Czarnecki et al., 2023). This enables not only an estimate of the total water content but also of its depth distribution. A more detailed description of the MSL/DAN instrument is provided in (Mitrofanov et al., 2012).

4. Simulation Tool and Setups

In this paper, we support our methodology and results on studying near-surface water with albedo protons with model calculations. For this purpose, we use "GEometry ANd Tracking" (Geant4) version 10.7.4 (Agostinelli et al., 2003; Allison et al., 2006, 2016), which is a Monte Carlo radiation transport code. We employ the FTFP_BERT_HP physics list, which combines the Bertini cascade model for hadrons at intermediate energies ($\lesssim$10 GeV) and the Fritiof string model at higher energies, ensuring accurate modeling of the broad GCR spectrum interacting with the regolith. The High Precision extension provides detailed neutron transport down to thermal energies, which is likewise essential for modeling secondary particle cascades in the soil.

The primary objective is to understand how the surface radiation environment interacts with the Martian soil, with specific focus on two key questions: (a) at which depths within the soil albedo protons are generated, thus up to which depths the WEH content can be probed, and (b) how strong the impact of the regolith water content is on the albedo proton flux. The latter will subsequently help characterize the measurement duration required by, for example, MSL/RAD to obtain a statistically significant estimate of the WEH content.

To address these questions, we simulate a 2 × 2 m section of Martian soil with a depth of 60 cm. This thickness of the regolith is sufficient to capture all protons capable of becoming albedo, ensuring that no upward-escaping secondary particles produced by primary or secondary interactions are lost through the back of a slab that is too thin (see Section 7, Figure 8). We model the Martian soil using pure quartz (SiO_2), as it is a major component of all igneous rocks found on Mars and on Earth. Although it is normally not present in its pure form, Zaman et al. (2021) have shown that the precise composition of heavier elements ($\geq$Oxygen) in dry soil (excluding water) has no significant effect on the spectra of charged albedo particles, which justifies our simplified scenario. This dry Martian soil is then combined with four different homogeneously distributed water contents, see Table 1, representing various possible scenarios found on Mars. Since WEH is defined as the weight percent of water that would be present if all hydrogen were in the form of H_2O (Tate et al., 2015), the densities ρ_{tot} of the hydrous scenarios are calculated as

$$\rho_{\mathrm{tot}} = \frac{m_{\mathrm{tot}}}{V_{\mathrm{tot}}} = \left(\frac{f_{\mathrm{Quartz}}}{\rho_{\mathrm{Quartz}}} + \frac{f_{\mathrm{Water}}}{\rho_{\mathrm{Water}}}\right)^{-1}, \tag{1}$$

where $\rho_{\mathrm{Water}} = 1.0\,\mathrm{g/cm^3}$ and $\rho_{\mathrm{Quartz}} = 2.8\,\mathrm{g/cm^3}$. The latter value was adopted for consistency with the simulation setup presented by Röstel et al. (2020). The respective weight fractions are denoted by f and satisfy the condition $f_{\mathrm{Water}} + f_{\mathrm{Quartz}} = 1$. All WEH values reported in the following refer to weight percent unless stated otherwise.

We test the response of the different subsurface scenarios to GCR protons and neutrons produced in the Martian atmosphere, as both together represent the major contribution to the radiation environment on the surface of Mars (see Section 1). Both particle types are simulated with an isotropic E^{-1} power-law distribution between 100 keV and 1 TeV to obtain a general response of albedo protons to incoming neutrons and protons. The source is a 2 × 2 m patch placed directly above the soil. The resulting albedo particles are captured by an infinitesimally thin detector, positioned centrally above both the surface and the source. The detector cannot have the same dimensions as the source and soil, as this would introduce undesired boundary effects, such as non-uniform surface exposure or non-isotropic detection of albedo particles. In a preliminary study, we found that a 40 × 40 cm detector is sufficient to maximize statistics without introducing such boundary effects.

Subsequently, we weight the proton and neutron input spectra with the corresponding realistic surface spectra presented in (Matthiä & Berger, 2017) to obtain realistic Martian albedo proton spectra. We do not use an atmospheric- or solar-cycle–varying input spectrum, as these effects can be corrected in our measurements (see Sections 5 and 6). Moreover, the rover body is not included in our simulations. On the one hand, because the exact composition of the rover body is not precisely known, and on the other hand, this allows the simulation results to remain as generally applicable as possible. Nevertheless, the influence of the rover body on the simulation results is addressed in Section 8.

5. Methodology

Signatures of protons with different directionalities in MSL/RAD have previously been investigated by Appel et al. (2018), using a methodology developed by McDonald and Ludwig (1964). Here, we adapt and refine this methodology for measurements on the surface of Mars. We exploit the fact that, according to the Bethe–Bloch equation (Bethe, 1930),

$$-\frac{\mathrm{d}E}{\mathrm{d}x} \sim \frac{mZ^2}{v^2}, \tag{2}$$

particles of the same species (identical mass m and atomic number Z) deposit more energy in a detector at lower velocities v, that is, the lower their kinetic energy. The protons entering MSL/RAD from above already deposit energy in detector D, denoted E_{D}, and consequently are slowed down, depositing more energy in detector E, denoted E_{E}. Protons entering MSL/RAD from below as albedo protons first deposit energy in detector E, are

Table 1

Quartz as the Martian Soil Material, Combined With Different Water Contents Added in Weight Percent Relative to the Quartz Mass, to Represent Various Scenarios at Different Latitudes on Mars

Soil f_{Quartz}	Water budget f_{Water}	Scenario	Latitude	Density $\rho\,[\mathrm{g/cm^3}]$
100% SiO_2	0% H_2O	Equator (dry)	~0°	2.8
80% SiO_2	20% H_2O	Near equator	±45°	2.058
60% SiO_2	40% H_2O	Local formations	±45°	1.628
40% SiO_2	60% H_2O	Poleward	±60°	1.347
20% SiO_2	80% H_2O	Planum Boreum & Planum Australe	±90°	1.147

Note. The density of each scenario, shown in the last column, is calculated according to Equation 1.

subsequently slowed down, and thus deposit more energy in detector D. From the ratio of E_D to E_E versus the total energy deposited in MSL/RAD, $E_{\mathrm{tot}} = E_{A2} + E_B + E_C + E_D + E_E$, the directions of protons can be distinguished in a so-called "fishplot." Since our analysis requires a hit in both detectors D and E, we use only the inner FOV A2 × B of MSL/RAD, where this condition is satisfied. Accordingly, we also apply the penetrating particle mask introduced in Section 3.1.

The MSL/RAD measurement between 13 January 2021 and 10 June 2022 (arbitrary time range for demonstration) is shown in Figure 3. Between $E_{\mathrm{tot}} \sim 45$–100 MeV, the upward branch, resulting from albedo protons, can be clearly distinguished from the downward branch, resulting from downstreaming protons. This corresponds to a primary proton energy of about $E_{\mathrm{prim}} \sim 100$–200 MeV, where "primary proton energy" refers to the proton energy before entering MSL/RAD. For primary proton energies $E_{\mathrm{prim}} \gtrsim 200$ MeV, corresponding to $E_{\mathrm{tot}} \lesssim 45$ MeV in MSL/RAD, the two branches merge into the "Minimal Ionizing Particle Species" (MIPS) peak. These particles are too energetic for directional dependencies to be inferred from the D-to-E ratio.

Using the same explanation as for protons, downstreaming and MIPS alpha particle signatures, as well as the branch of downstreaming deuterons, can also be identified in Figure 3. Although predicted by model results from Guo, Banjac, et al. (2019), no signatures of albedo deuterons or albedo alpha particles resulting from GCR and atmospheric-secondary interactions with the soil are observed at the Martian surface with MSL/RAD, suggesting that these particles are fully absorbed within the rover body.

A major challenge in isolating albedo protons is their contamination by the MIPS peak of alpha particles. Since we aim to study albedo protons exclusively in relation to the WEH content in the soil, this contamination must be effectively filtered out. To achieve this, we introduce a two-level procedure. First, we define a polygonal mask to separate albedo protons from downstreaming protons and to remove the majority of alpha particles. The polygonal mask is depicted as the highlighted region in Figure 4. The alpha particle contamination that falls within the polygonal mask is filtered out in a second step using an integration line technique. The tip of the alpha particle MIPS contamination is modeled with a quadratic Bézier curve (Baydas & Karakas, 2019), computed separately in the x and y directions as follows:

$$P(t) = (1-t)^2 P_0 + 2(1-t)tP_1 + t^2 P_2 \,, \tag{3}$$

where P_0 and P_2 are the respective start and end points, and P_1 defines the curvature of the contamination. This modulated integration line is then shifted from lower to higher E_{tot}, effectively moving the integration line from the region of pure albedo proton counts to the part of the proton counts contaminated by alpha particles. The shifting procedure of the integration line is illustrated in Figure 4, and the resulting counts per integration slice are shown in the subplot above. A clear separation between the pure albedo proton signal and the alpha particle–contaminated albedo proton signal can be observed.

On larger timescales, as shown in Figure 4, both components can be well fitted with Gaussian functions to estimate the statistics of albedo protons as well as the alpha particles that still fall within the first-level selection polygonal mask. However, the Curiosity rover is constantly moving and may therefore traverse regions where the water content varies considerably over short periods. Due to the limited statistics on such timescales, we therefore choose to introduce a cutoff between the two signals instead. Although this approach does not capture all possible

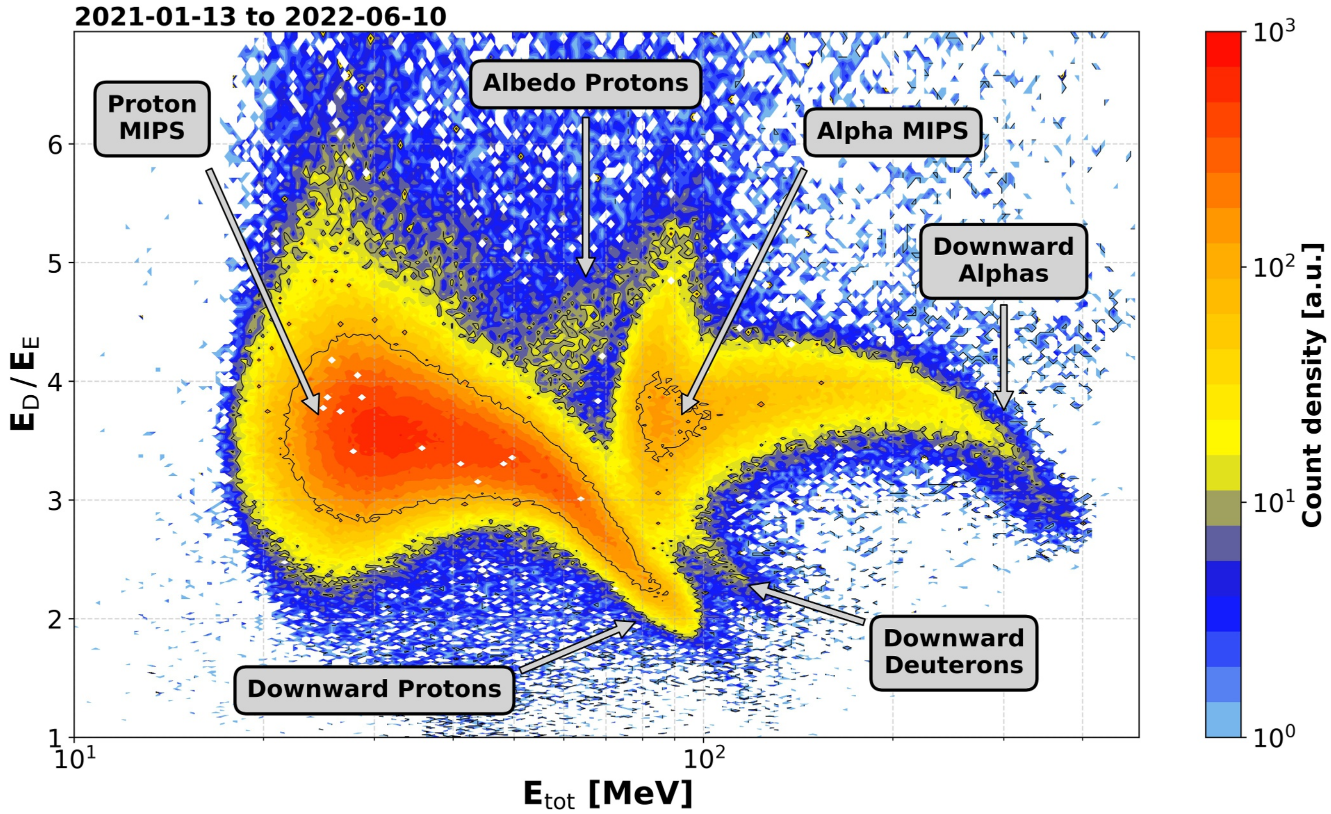

Figure 3. The energy deposit ratio E_D/E_E versus the total energy deposit E_{tot} measured by Mars science laboratory/radiation assessment detector over approximately one and a half years during solar minimum. Distinct signatures of protons, alphas, and deuterons can be identified.

albedo protons, it ensures a more purified albedo proton signal for studying the WEH content in the regolith on shorter timescales. The purple-shaded region in Figure 4 contains the albedo counts that are missed by this cutoff methodology. The green-shaded region represents the part that remains contaminated by alpha particles even after the two-level cutoff procedure. Although the Gaussian fitting is not applied further, it still helps to estimate the latter. We perform a Monte Carlo integration of this region over different time intervals on Mars of approximately one and a half years each, rather than over the entire measurement period, since the contamination may vary over time and under different solar conditions. The resulting uncertainty is then assigned to our measurements, ranging from 4.45% to 7.23% of the total albedo proton counts. Due to the two-level cutoff procedure, the specific choice of the polygonal mask in the first level has only a minor influence on the resulting albedo proton signal. Toward lower E_{tot}, the mask is constrained by the simulation results of Appel et al. (2018). Extending the mask toward higher E_{tot} increases contamination, that is, the alpha peak becomes larger. However, this contribution is fitted and removed in the second-level cut. Although this does not affect the albedo proton counts itself, it may influence the uncertainty assigned to the measured albedo protons through the Monte Carlo integration. As a cross-check, we applied a broader polygonal mask and obtained uncertainties of the same order of magnitude as reported here. The applied polygonal masks are available on Zenodo for reproducibility (Löwe, 2026).

In order to investigate the water content in the Martian regolith we additionally have to ensure that the albedo protons are not influenced by other effects such as atmospheric pressure variations on Mars or solar modulation or that we can correct these unwanted variations. Therefore, we also capture the downstreaming and MIPS proton component, highlighted and labeled as "GCR Protons" in Figure 4, to normalize these effects. Since MSL/RAD can detect albedo protons with energies of approximately 100–200 MeV, the particles interacting with the Martian soil must possess at least this energy or higher. All downstreaming and MIPS protons within the highlighted mask satisfy this condition and are thus representative of the particles capable of producing albedo protons on Mars. The idea is that any variation in these input particles has a proportional effect on the albedo proton spectrum, allowing us to filter out such variations (see Section 6). Thus, the higher the input flux, the higher the albedo proton flux, and vice versa. With this framework, we have assembled all the necessary ingredients to measure

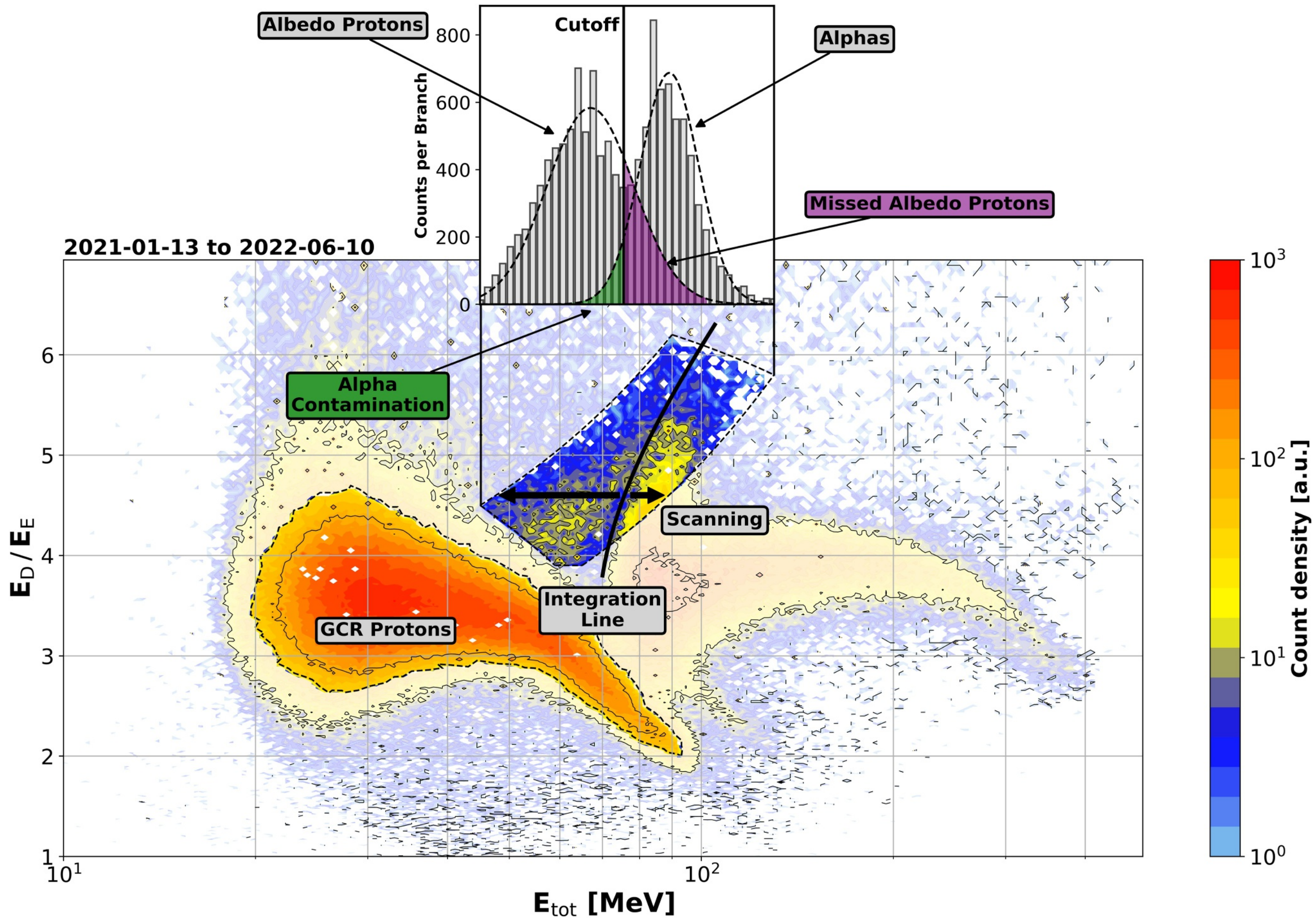

Figure 4. Same spectra plot as in Figure 3, but with a focus on the MIPS and downstreaming proton part, labeled as "GCR Protons," as well as an illustration of the two-level selection procedure used to obtain albedo protons. A clear separation between albedo protons and alpha particles after the two-level selection procedure is visible in the subplot. The green-shaded area represents the residual alpha-particle contamination of the albedo protons after the applied cutoff.

albedo protons with MSL/RAD as a single instrument, ensuring that they presumably depend solely on variations in the Martian soil composition.

6. Results

The daily MSL/RAD measurements from 6 March 2016 to 3 April 2025 are plotted in Figure 5. The first panel shows the integrated flux of downstreaming and MIPS protons $\mathcal{F}_{\mathrm{p,GCR}}$. The dependence on solar activity is evident, resulting in a higher flux during solar minimum and a lower flux during solar maximum.

The second panel in Figure 5 shows the integrated albedo proton flux $\mathcal{F}_{\mathrm{p,alb}}$, derived using the two-level cutoff method described in Section 5. A weak dependence on solar activity is also observed, although it is less pronounced than for $\mathcal{F}_{\mathrm{p,GCR}}$. The reason is that albedo protons observed here are produced by mainly GCR protons with higher energies which do not significantly depend on the solar cycle. Irregular spikes in the measurements may occur due to microphonics, typically associated with rover drilling activities or movements of the rover arm during, for example, operation of the dust removal tool or measurements with the Alpha Particle X-ray Spectrometer (APXS; Gellert et al., 2009). SEP events do not always appear to affect the albedo proton flux. However, we exclude them as a precaution, since the increased particle flux during an SEP event could, in theory, also lead to an enhanced albedo proton flux independent of the soil composition. A total of 12 SEP events occurred during our observation period from 6 March 2016 to 3 April 2025, as documented in (Löwe et al., 2025; Posner et al., 2025). Consequently, 31 days were removed in total from the data set spanning more than 9 years of measurements.

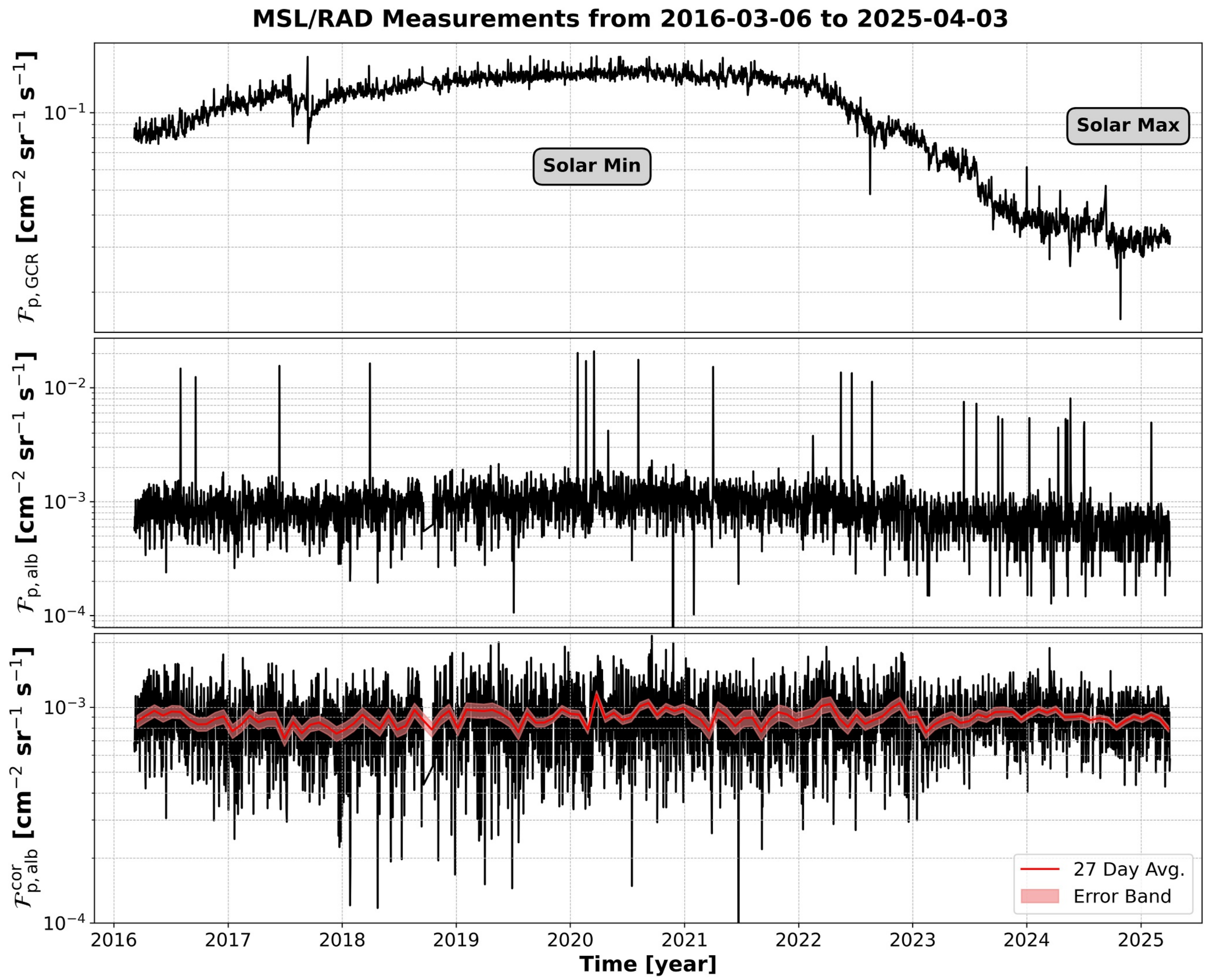

Figure 5. The first panel depicts the integrated particle flux from MIPS and downstreaming protons $\mathcal{F}_{\mathrm{p,GCR}}$, including all particles falling within the highlighted "GCR Protons" mask in Figure 4. The second panel shows the integrated albedo proton flux $\mathcal{F}_{\mathrm{p,alb}}$. Peaks in the measurements represent outliers, mainly associated with rover drilling or arm activity, as well as solar energetic particle events. The error band is too small to be resolved visually and is therefore omitted. The third panel shows the integrated albedo proton flux corrected for solar modulation and pressure changes $\mathcal{F}^{\mathrm{cor}}_{\mathrm{p,alb}}$. More details on the detrending are provided in the text. For clarity, the error band after correction is plotted only for the red 27-day average. Variations in $\mathcal{F}^{\mathrm{cor}}_{\mathrm{p,alb}}$ are assumed to depend primarily on changes of the WEH content in the soil.

The third panel in Figure 5 depicts the albedo proton flux measured by MSL/RAD, with outliers removed as well as corrected for solar modulation and long-term atmospheric effects. The latter is obtained by plotting the input flux, $\mathcal{F}_{\mathrm{p,GCR}}$, against the albedo proton flux, $\mathcal{F}_{\mathrm{p,alb}}$, using a 27-day moving average over a solar Bartels rotation (Bartels, 1934), as shown in Figure 6. The error bars of $\mathcal{F}_{\mathrm{p,GCR}}$ represent the statistical uncertainty, while the error bars of $\mathcal{F}_{\mathrm{p,alb}}$ account for both the statistical uncertainty and the estimated contamination from alpha particles. The statistical uncertainty was derived from Poisson counting statistics of the detected events within each 27-day interval and propagated to the corresponding flux values.

As anticipated in Section 5, both fluxes exhibit a clear linear correlation. The best-fit line is determined using orthogonal distance regression (Boggs & Rogers, 1990), taking into account the uncertainties in both fluxes $\mathcal{F}_{\mathrm{p,GCR}}$ and $\mathcal{F}_{\mathrm{p,alb}}$. The Pearson correlation coefficient and its uncertainty are $r = 0.823 \pm 0.021$, computed using a bootstrapping method (Efron & Tibshirani, 1994; Hall, 1992), in which the data uncertainties are randomly resampled 5,000 times following a normal distribution to estimate their impact on the correlation. The p-value corresponding to the correlation coefficient is obtained by propagating the uncertainty in r, yielding

$p = (8.08 \pm 0.53) \times 10^{-31}$. Together, both values underline the clear positive correlation between the two quantities. The gray-shaded area represents the 95% confidence interval of the fit, while the yellow-shaded region indicates the prediction interval. The resulting fit parameters are a slope of $(3.92 \pm 0.14) \times 10^{-3}$ and an intercept of $(4.85 \pm 0.14) \times 10^{-4}$ $\mathrm{cm^{-2} s^{-1} sr^{-1}}$.

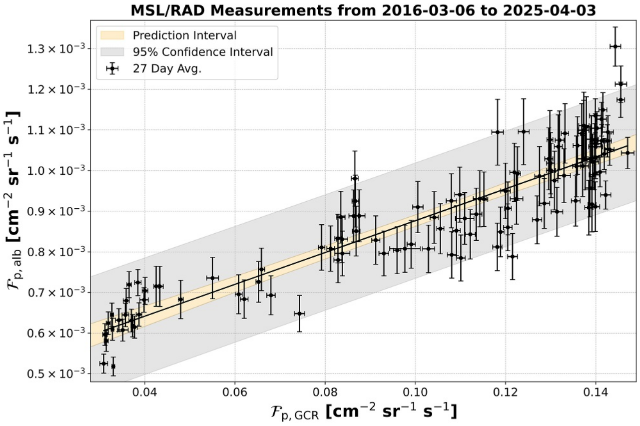

Figure 6. Linear correlation between the MIPS and downward proton flux $\mathcal{F}_{\mathrm{p,GCR}}$ and the albedo proton flux $\mathcal{F}_{\mathrm{p,alb}}$. This analysis is used to remove the effects of solar modulation from $\mathcal{F}_{\mathrm{p,alb}}$.

Subsequently, we correct the albedo proton flux, $\mathcal{F}_{\mathrm{p,alb}}$, for solar modulation and long-term atmospheric effect according to

$$\mathcal{F}^{\mathrm{cor}}_{\mathrm{p,alb}} = \mathcal{F}_{\mathrm{p,alb}} - \mathrm{slope} \cdot \left(\mathcal{F}_{\mathrm{p,GCR}} - \overline{\mathcal{F}_{\mathrm{p,GCR}}}\right) \tag{4}$$

which is shown in the third panel of Figure 5. The mean corrected albedo proton flux over the entire measurement period is $\overline{\mathcal{F}^{\mathrm{cor}}_{\mathrm{p,alb}}} = 8.9 \cdot 10^{-4}$ $\mathrm{cm^{-2}}$ $\mathrm{sr^{-1} s^{-1}}$. The associated uncertainty ranges from 4% to 12% and is shown only for the 27-day averaged curve for clarity, with a mean error of 6.3%. It is derived by propagating the uncertainties in Equation 4, taking into account the fit uncertainty of the slope, the statistical error of $\mathcal{F}_{\mathrm{p,GCR}}$, and the combination of statistical and alpha particle contamination uncertainties for $\mathcal{F}_{\mathrm{p,alb}}$.

As a sanity check, we compared the albedo proton flux both before and after correction with $\mathcal{F}_{\mathrm{p,GCR}}$ to atmospheric pressure data measured by the Rover Environmental Monitoring Station (REMS; Gómez-Elvira et al., 2012), also onboard MSL. In both cases, no correlation was found. The latter is expected, as this effect cancels out through the correction with the input spectrum. The former indicates that atmospheric pressure variations do not significantly influence the albedo proton flux measured by MSL/RAD in the first place, since albedo protons are detected at energies of 100–200 MeV, which can only be produced by interactions of higher-energy particles with the regolith. As noted in Section 2, this corresponds exactly to the GCR energy range that reaches the Martian surface directly, without significant interaction with the atmosphere. Consequently, the variations shown in the third panel of Figure 5 are assumed to depend solely on the water budget in the soil, rather than on other effects.

To determine whether the small fluctuations in $\mathcal{F}^{\mathrm{cor}}_{\mathrm{p,alb}}$ can be attributed to variations in the WEH content of the soil, we group our measurements according to different local and global formations traversed by the Curiosity rover, within which the WEH content of the soil is presumed to remain approximately constant. $\mathcal{F}^{\mathrm{cor}}_{\mathrm{p,alb}}$ assigned to the local formations is depicted in the first panel of Figure 7, with the global formations color-coded. The black line within each box represents the mean value of the local formation, while the box itself corresponds to the interquartile range (IQR). The whiskers extend from the 5th to the 95th percentile of the measurements.

The highest corrected albedo proton flux is measured at the Stimson Formation ($\overline{\mathcal{F}^{\mathrm{cor}}_{\mathrm{p,alb}}}[\mathrm{Stimson}] = 9.76 \cdot 10^{-4}$ $\mathrm{cm^{-2}\ sr^{-1}\ s^{-1}}$) and at Catrimani ($\overline{\mathcal{F}^{\mathrm{cor}}_{\mathrm{p,alb}}}[\mathrm{Catrimani}] = 9.85 \cdot 10^{-4}$ $\mathrm{cm^{-2}\ sr^{-1}\ s^{-1}}$). The former deviates by +9.7% and the latter by +10.7% from the mean flux over the entire measurement period. The lowest corrected albedo proton flux is observed at Pettegrove Point ($\overline{\mathcal{F}^{\mathrm{cor}}_{\mathrm{p,alb}}}[\mathrm{PettegrovePoint}] = 8.18 \cdot 10^{-4}$ $\mathrm{cm^{-2}\ sr^{-1}\ s^{-1}}$) and Amapari ($\overline{\mathcal{F}^{\mathrm{cor}}_{\mathrm{p,alb}}}[\mathrm{Amapari}] = 8.22 \cdot 10^{-4}$ $\mathrm{cm^{-2}\ sr^{-1}\ s^{-1}}$). The former deviates by −8% and the latter by −7.6% from the mean flux over the entire measurement period. As discussed in Section 2, this would suggest that the soil in the Stimson Formation and in Catrimani is relatively drier, whereas the soil at Pettegrove Point and Amapari appears more hydrous compared to the other local formations. However, when the measurement uncertainties are taken into account, these variations between the formations are not statistically significant.

Furthermore, we compare the MSL/RAD measurements with MSL/DAN observations of subsurface WEH content in the same formations, as shown in the second panel of Figure 7. The WEH content is derived from MSL/DAN passive measurements According to these results, subsurface WEH varies only weakly among the formations, ranging from approximately 2% to 7%. The highest water content is measured in the Catrimani Formation with 5.7%, while the lowest (excluding Pahrump Hills, where no MSL/RAD data are available) is observed in the Stimson Formation with 2.5%. MSL/RAD should measure a higher corrected albedo proton flux when MSL/DAN observes a lower subsurface WEH content, and conversely, a lower corrected albedo proton flux

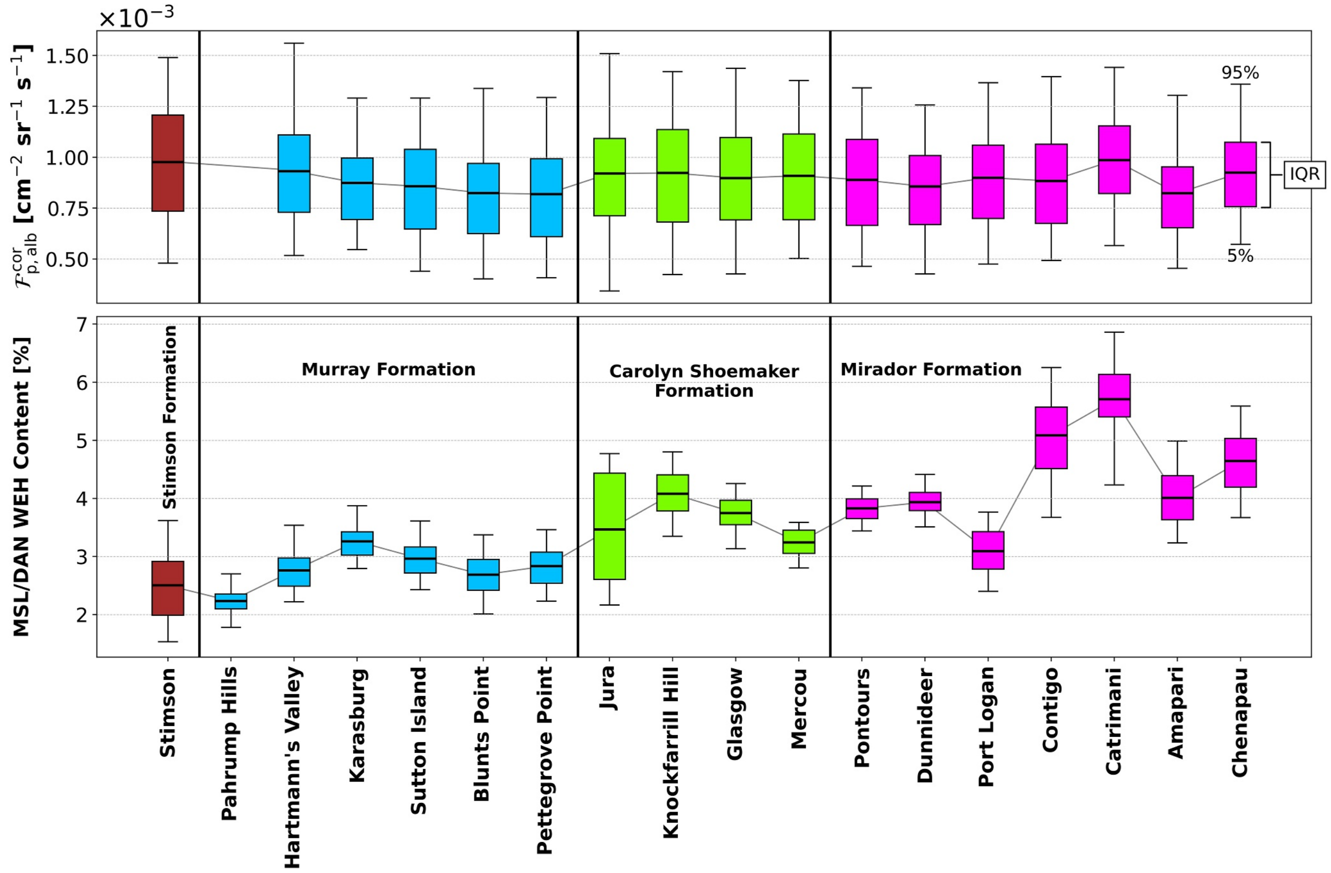

Figure 7. The upper panel shows the corrected albedo proton flux $\overline{\mathcal{F}_{\mathrm{p,alb}}^{\mathrm{cor}}}$ measured by Mars science laboratory (MSL)/radiation assessment detector (RAD) across different local formations, with global formations color-coded. The lower panel presents the subsurface WEH content measured by MSL/dynamic albedo of neutrons (DAN) and is an extended data set presented in Nikiforov et al. (2024), provided by the MSL/DAN team itself. The boxes indicate the interquartile range, and the whiskers correspond to the 5th and 95th percentiles of the measurements. If MSL/DAN measures a lower WEH content, MSL/RAD is expected to observe a higher albedo proton flux, and vice versa.

when MSL/DAN measures a higher subsurface WEH content. However, no anticorrelation between the MSL/RAD and MSL/DAN measurements can be observed within the individual formations. For example, the measurements in the Stimson Formation even exhibit the opposite trend to that expected. We also compared the daily measurements from MSL/RAD and MSL/DAN, as well as the MSL/RAD measurements grouped according to the different WEH contents measured by MSL/DAN. In both cases, no significant anticorrelation was observed.

The lack of an observed anticorrelation between MSL/RAD and MSL/DAN may be explained as follows: One possible reason is that MSL/RAD and MSL/DAN probe the soil WEH content at different depths, which can lead to differing results. MSL/DAN measures the WEH content via albedo neutrons, which are sensitive to depths of up to approximately one m, whereas MSL/RAD measures the WEH content via albedo protons, which are sensitive to the uppermost regolith layer of a few centimeters, see Section 4. Another explanation is that variations in soil WEH content of 2%–7% may simply be too small to be detected by MSL/RAD albedo protons, probably because (a) the albedo proton flux does not respond significantly to such small WEH variations, (b) changes in the albedo proton flux due to these small WEH variations are overlapped by other effects unrelated to soil composition that we cannot filter out, (c) MSL/RAD's restricted FOV and continuous rover motion limits the counting statistic, although longer measurement durations might have allowed MSL/RAD to resolve these small WEH differences, or (d) MSL/RAD is mounted on top of the Curiosity rover, and shielding by the rover body limits the attribution of the albedo proton flux to the soil WEH content. A more detailed discussion of the measurement results, including relevant caveats, is provided in Section 8.

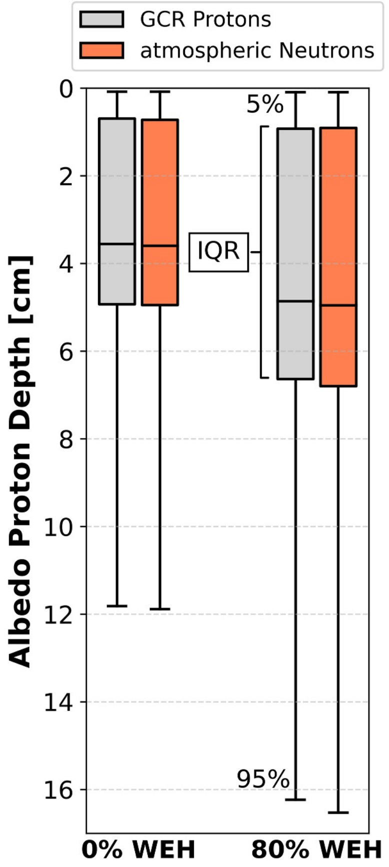

Figure 8. Production depth of albedo protons for the two boundary cases of 0% and 80% soil WEH content, distinguishing between interactions of Galactic Cosmic Ray protons and atmosphere-produced neutrons with the Martian soil.

In the following Section 7, we will therefore use supporting model calculations to investigate the depths to which albedo protons can provide information on the regolith water budget and to determine the sensitivity limits of MSL/RAD with respect to the WEH content.

7. Simulation Results

In this section, we use the simulation setup described in Section 4. First, we investigate the depths at which albedo protons are produced, that is, up to which depths conclusions about the WEH content in the soil can be drawn. In Figure 8, the depths at which albedo protons are produced are shown for the two boundary cases of soil with 0% and 80% WEH content. These protons, expected at the Martian surface as a result of interactions of GCR protons and atmospheric secondary neutrons with the soil, are indicated in gray and orange, respectively. Analogous to Figure 7, the boxes represent the IQR, and the whiskers indicate the 5%–95% percentile of the data. The results include all albedo protons, regardless of their energy when leaving the soil. As a first result, the production depth of albedo protons is nearly independent of whether they are generated by an incoming proton or neutron. This is initially surprising, since protons have a much shorter range in soil due to ionization losses than neutrons, which can penetrate deeper into the ground. However, upward-directed protons at greater depths must still traverse the same distance upward to escape the soil. Due to their high energy loss, they consequently remain trapped within the soil rather than becoming albedo protons, resulting in only minor differences in production depth compared to those generated by incident GCR protons. The average production depth at 0% WEH content is approximately 3.5 cm, with the IQR ranging from 0.7 to 5 cm. Only occasionally do albedo protons originate from greater depths of about 12 cm (upper 95% percentile) or from the very top layer at depths as shallow as 0.7 mm (lower 5% percentile). The production depth depends only slightly on the WEH content in the soil. For the extreme case of 80% WEH content, the mean production depth of albedo protons is 4.9 cm, with an IQR ranging from approximately 0.9–6.6 cm. The lower 5% percentile is around 0.9 mm, while the upper 95% percentile reaches 16 cm. Thus, at a higher WEH content, albedo protons may originate from slightly greater depths, although this effect remains marginal.

The dependence of the production depth on albedo proton energy shows only a very minor effect and is discussed in Supporting Information S1. The observed trend indicates that for low albedo proton energies below 100 MeV (mean 2.5 cm at 0% WEH and 3.6 cm at 80% WEH) and for high albedo proton energies above 1 GeV (mean 2.7 cm at 0% WEH and 3.2 cm at 80% WEH), the production depth becomes smaller. The former occurs because the primary particles do not penetrate deeply into the soil, while the latter results from the primary particles penetrating so deeply that the produced upward-directed protons remain trapped in the soil and do not become albedo protons. Albedo protons with energies between 100 and 500 MeV are produced at the greatest depths. This range also includes the MSL/RAD-sensitive energy interval of 100–200 MeV, where at 0% WEH content they are generated within an IQR depth range of 0.95–5.44 cm (mean: 3.96 cm), and at 80% WEH content within an IQR depth range of 1.43–7.68 cm (mean: 5.65 cm).

Albedo protons are therefore suitable for investigating near-surface water because of their ability to probe beneath an upper dust and rock layer that hinders optical detection of WEH content. Moreover, this study provides access to different depth ranges compared to existing methods using albedo neutrons or albedo gamma rays, both being sensitive to depths of about 60 cm below the Martian surface (see Section 2).

The differential flux of albedo protons on the surface of Mars resulting from the simulation setup is shown in Figure 9, color-coded for the different subsurface water scenarios from Table 1. These fluxes arise from the combination of the downward neutron spectrum (solid gray line) and the downward GCR proton spectrum (solid black line) modeled by Matthiä and Berger (2017) on the surface of Mars. The dashed black line represents the

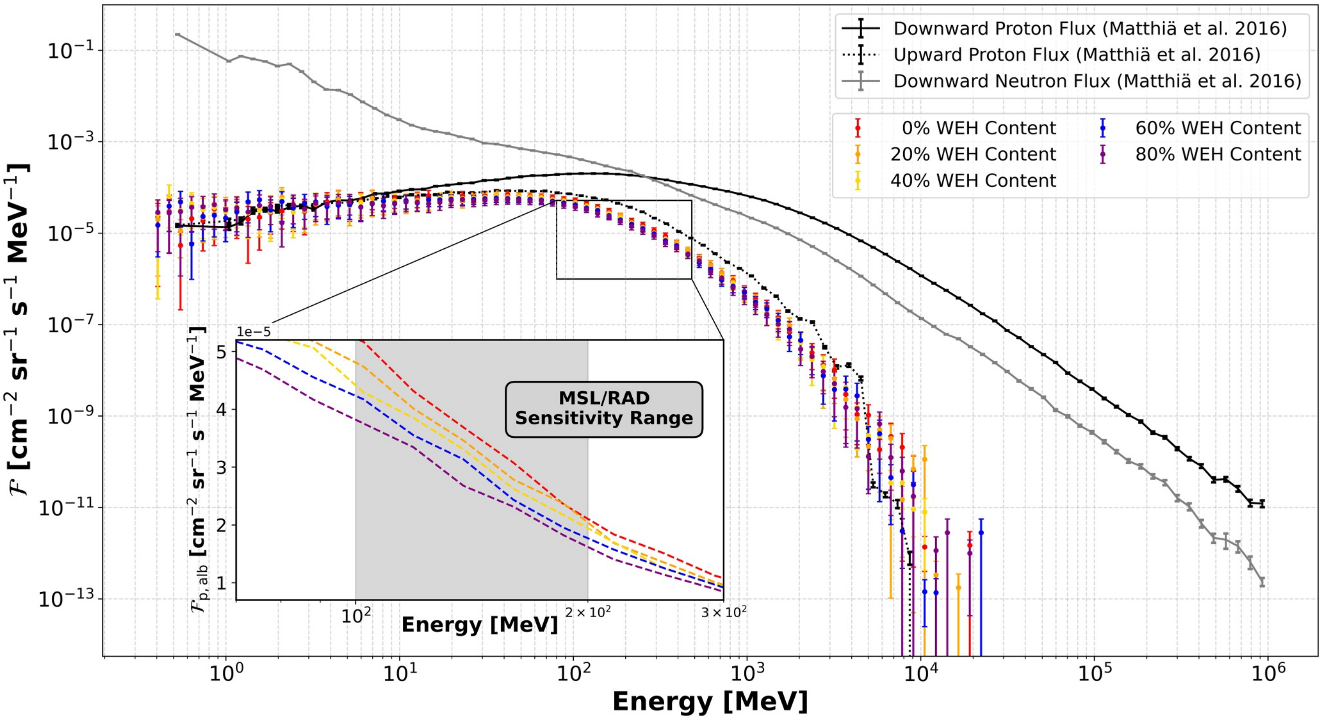

Figure 9. Differential particle fluxes on the surface of Mars. Solid lines show the downward neutron and proton spectra from (Matthiä & Berger, 2017), while the colored spectra represent our resulting albedo proton fluxes for different WEH contents. The zoomed-in plot highlights the 100–200 MeV range, where albedo protons can be clearly identified in Mars science laboratory/radiation assessment detector.

simulated albedo proton spectrum from (Matthiä & Berger, 2017) and serves as a cross-check for our simulation. Our results agree well with the literature, particularly for energies up to 100 MeV. The small deviations of the spectra at energies above 100 MeV are due to our simulation including only neutrons and protons, while additional heavier ions considered in (Matthiä & Berger, 2017) were omitted. These heavier ions can further contribute to albedo proton production, leading to a slightly higher flux.

The albedo proton spectra for the five different soil water scenarios support the trend described in Section 2: A suppression of albedo proton fluxes at higher WEH content, particularly visible in the zoomed-in plot in Figure 9. The expected integrated albedo flux in the MSL/RAD-sensitive energy range of 100–200 MeV for the four different water scenarios is listed in Table 2.

With a model predicted integrated flux of approximately $3.74 \cdot 10^{-3}$ cm^{-2} sr^{-1}s^{-1} for the 0% WEH content scenario, representative of conditions along the MSL path, this value exceeds the flux measured by MSL/RAD, which averages $0.9 \cdot 10^{-3}$ cm^{-2} sr^{-1}s^{-1}. This discrepancy is expected because the measurement is not performed in the idealized environment of the simulation. Instead, it is affected by contamination from alpha particles, which

Table 2
Expected Albedo Proton Flux in the MSL/RAD-Sensitive Energy Range From 100 to 200 MeV on the Surface of Mars for Different Soil WEH Contents

WEH content	Scenario	Integrated flux (100–200 MeV)	Reduction (vs. dry)
0%	Equator (dry)	3.70×10^{-3} cm^{-2} s^{-1} sr^{-1}	0.0%
20%	Near Equator	3.47×10^{-3} cm^{-2} s^{-1} sr^{-1}	−6.2%
40%	Local Formations	3.25×10^{-3} cm^{-2} s^{-1} sr^{-1}	−12.2%
60%	Poleward	3.04×10^{-3} cm^{-2} s^{-1} sr^{-1}	−17.8%
80%	Planum Boreum & Planum Australe	2.78×10^{-3} cm^{-2} s^{-1} sr^{-1}	−24.9%

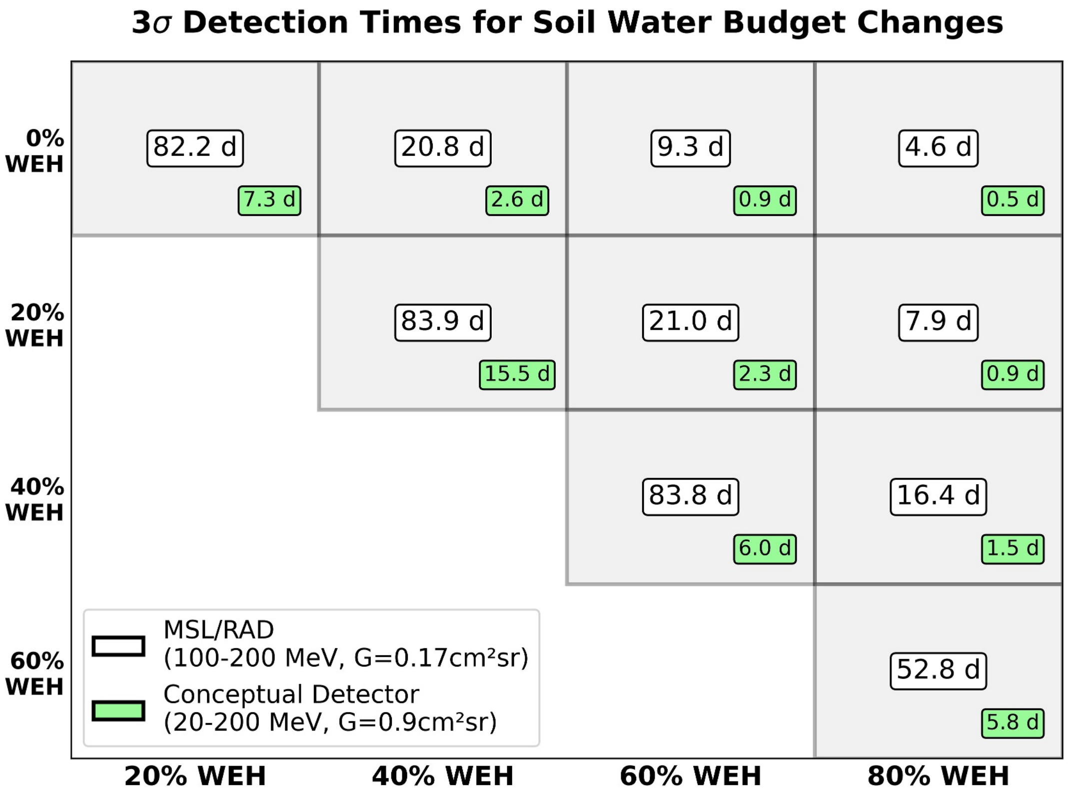

Figure 10. Matrix of measurement time required to achieve a 3σ detection of variations in the water content of Martian soil. The five scenarios from Table 1 were considered. Numbers in the white boxes correspond to measurements with Mars science laboratory/radiation assessment detector, while numbers in the green boxes correspond to a potential future detector.

are removed in our two-step procedure, leading to the rejection of some albedo protons. In addition, and in contrast to the simulation, albedo protons penetrate the rover body before being detected by MSL/RAD, which may further reduce the measured flux (see Section 8 for further discussion).

Nonetheless, a clear suppression of the integrated flux between 100 and 200 MeV is evident. For instance, the albedo proton flux is expected to decrease by approximately 6% if MSL transitions from completely dry soil to a water-rich formation with 20% WEH, as found, for example, in Arabia Terra or Arcadia Planitia. In local formations with about 40% WEH, such as the Medusae Fossae Formation, our model predicts a suppression of approximately 12%. A reduction of the albedo proton flux between 100 and 200 MeV of approximately 25% is estimated at the hydrous polar regions compared to the dry near-equatorial regions (cf. Table 2).

The question now is how long measurements would need to be accumulated in order to statistically distinguish the differences in albedo proton fluxes between the various soil water scenarios. We perform a two-sample hypothesis test assuming Poisson statistics, which allows the required measurement time T for a 3σ detection of varying WEH content to be calculated as

$$T = \frac{z^2}{G}\,\frac{\int_{E_{\min}}^{E_{\max}} \mathcal{F}_{\mathrm{i}}\mathrm{d}E + \int_{E_{\min}}^{E_{\max}} \mathcal{F}_{\mathrm{j}}\mathrm{d}E}{\left(\int_{E_{\min}}^{E_{\max}} \mathcal{F}_{\mathrm{i}}\mathrm{d}E - \int_{E_{\min}}^{E_{\max}} \mathcal{F}_{\mathrm{j}}\mathrm{d}E\right)^2}, \tag{5}$$

where $z = 3$, G is the geometrical factor of the detector, and $\mathcal{F}_{i,j}$ are the albedo proton fluxes for two different WEH contents in the Martian soil. The energy limits within which albedo protons can be measured are denoted as $E_{\min}$ and $E_{\max}$. Using the geometrical factor and energy range of MSL/RAD, as described in Section 3.1, we calculate the required measurement time for different soil water budgets. These are illustrated as a combination matrix of the different scenarios from Table 1 in Figure 10.

The simulation results shown in Figure 10 suggest that a 20% variation in soil WEH content could be detected at the 3σ level by MSL/RAD within approximately two to 3 months. Specifically, if MSL/RAD were to traverse from its current location with approximately 0% WEH content to a latitude of 45°, local soil WEH contents of about 20% could be detected after roughly 83 days. This explains why signatures of water content changes of only 2%–7% could not be resolved in the MSL/RAD measurements, as detecting such small variations would have required substantially longer measurement times. Consequently, alongside comparisons with MSL/DAN data, this provides further evidence that the already statistically insignificant variations observed in MSL/RAD measurements of the albedo proton flux do not indicate real changes in WEH content, but are purely driven by statistical fluctuations.

A measurement period of approximately 3 months to resolve 20% variations in soil WEH content may initially appear long. However, it remains reasonable for an extended mission such as MSL/RAD, which has been operating for over 12 years. Moreover, localized water-rich formations with up to 40% WEH content, such as Tharsis Montes or the Medusae Fossae Formation, could likely be detected much earlier, requiring measurement times of only ~20 days as the rover traverses these regions. If the rover were to travel from the dry equator toward the poles, soil water contents of approximately 60% and potentially up to 80% could be detected within only ~9 days and ~5 days, respectively. However, this represents a somewhat idealized scenario that is not achievable within the MSL mission.

MSL/RAD was not originally designed for albedo particle detection or for the investigation of WEH content in the Martian soil. Nevertheless, the simulation results suggest promising measurement times for resolving different water budget scenarios on Mars using MSL/RAD. Therefore, we also investigated the expected measurement times of a realistically redesigned MSL/RAD detector that would be better suited for the detection of albedo protons. This conceptual detector would have a geometry factor of $0.9\ \mathrm{cm}^2\mathrm{sr}$, adapted from the alternative FOV A × B of MSL/RAD, and would be capable of measuring albedo protons over a broader energy range from 20 to 200 MeV. Furthermore, we require a clear FOV directed toward the soil, unobstructed by, for example, the rover body. The measurement times obtained with this conceptual detector are additionally shown in green in Figure 10. Such a detector would require only about 7 days of measurements to detect a change in soil WEH content of 20%, which is realistic, for example, for regions such as Arcadia Planitia or Arabia Terra. Local formations with 40% WEH content, such as the Medusae Fossae Formation, could accordingly be identified within approximately 2–3 days. Both correspond to reasonable distances traversable by rover or rotorcraft. Even larger variations of 60% or more would be detected almost instantaneously within about one day at the 3σ level.

8. Discussion

Measuring soil WEH content using albedo protons is a highly sensitive analysis. Therefore, both the measurements and the simulation results must be discussed and carefully contextualized.

Starting from the measurement results (see Section 6), we show that the albedo proton flux $\mathcal{F}_{\mathrm{p,alb}}$ can be corrected for solar modulation and potential atmospheric effects using the GCR proton flux $\mathcal{F}_{\mathrm{p,GCR}}$. The Pearson coefficient $r = 0.823 \pm 0.021$ indicates a clear correlation between them. Although such effects are not expected to be significant, contributions from heavier ions, which can also generate albedo protons and cause deviations from the GCR proton flux, are not explicitly included in the analysis. We subsequently assume that the corrected albedo proton flux depends solely on the WEH content of the Martian soil. However, rover inclination and surface roughness may induce small variations in the albedo proton flux that are not accounted for in this study. Additional topographic effects on the albedo proton flux, such as parking near or traversing past buttes (cf., e.g., Dibb et al., 2024; Guo, Khaksarighiri, et al., 2021), must be treated with caution to avoid misinterpreting these effects as variations in WEH content. A further limitation is that albedo protons must first penetrate the rover body before reaching MSL/RAD. This shielding can both modulate the incoming albedo proton flux and produce secondary protons that are indistinguishable from primary albedo protons associated with the WEH content. Such effects cannot be separated using measurements alone and may introduce additional uncertainties.

The simulation results were obtained under idealized conditions and are only valid within this framework. The rover is assumed to be on a perfectly flat surface, so surface roughness, topography, and rover inclination are not considered. Additionally, the water content is assumed to be homogeneously distributed within the soil. In reality, near-surface water may be in-homogeneously distributed, which could affect the albedo proton flux. Additionally, both quartz and typical Martian soil are assumed to have densities lower than the value of 2.8 g/cm^3 used in the simulation (Goossens et al., 2017; Mellon et al., 2022; P. Morgan et al., 2018). This difference has only a minor impact on the production depth of albedo protons (see Figure 8), but may lead to a smaller reduction in albedo proton flux between dry and hydrous soil than reported in Table 2. Furthermore, the rover body was not included in our simulation because its composition is not precisely known and we aimed to keep the results as general as possible. Nevertheless, Appel et al. (2018) demonstrated that the rover body can significantly reduce the albedo proton flux below 300 MeV compared to the unshielded flux, including the 100–200 MeV range measured by MSL/RAD. The rover body could also modulate albedo protons to lower energies. Consequently, the upward-directed protons detected by MSL/RAD likely do not correspond exactly to 100–200 MeV albedo protons leaving the soil, but rather to slightly higher-energy protons. In addition, the simulation assumes that MSL/RAD can detect all 100–200 MeV protons. As shown in Section 5, MSL/RAD measurements are contaminated by alpha particles, which we remove using the two-level cutoff procedure to obtain a pure albedo proton signal. This procedure inevitably results in the loss of a portion of the albedo proton data, which is not accounted for in the simulation. Both the influence of the rover body and the contamination by alpha particles are the main factors causing the measured albedo proton flux to be lower than the simulated flux (see Section 7). Therefore, the expected measurement times for MSL/RAD to resolve different WEH contents, shown in Figure 10, should be treated with caution and considered conservative lower limits, which would likely be significantly longer in reality.

Complementary, for the conceptual detector, an unobstructed FOV toward the soil and uncontaminated measurements of albedo protons are assumed, so the measurement times shown in Figure 10 are more reasonable. In reality, these times could even be shorter, because our simulation only accounts for albedo protons produced by the interaction of GCR protons and atmospheric neutrons with the soil, and not those from heavier ions, which would slightly increase the albedo proton flux (see Figure 9). Accordingly, we consider detecting variable WEH content with MSL/RAD using albedo protons highly challenging. A realistically redesigned detector could, however, provide a highly promising complement to other methods for investigating soil water content on Mars, the Moon, or other extraterrestrial bodies.

9. Conclusion

Investigating the water budget in the Martian soil has important implications, particularly for future manned missions to Mars, for understanding the history of the planet, and for the potential detection of ancient or extant microorganisms. In this study, we investigate whether albedo protons generated by the interaction of GCRs with Martian soil can be used to detect near-surface water reservoirs. A lower albedo proton flux is expected for higher soil water content and vise versa. Our results show that albedo protons are generated at depths of roughly 3–7 cm, allowing near-surface water to be probed even beneath dust layers that hinder optical detection. This would establish a new sensitivity depth range complementary to existing albedo neutron and gamma-ray measurements.

Therefore, we developed a methodology to detect albedo protons in the 100–200 MeV range using the RAD onboard the MSL. Contamination from alpha particles is removed via a two-level cutoff procedure. Subsequently, effects independent of soil composition, such as solar modulation and atmospheric pressure variations, are corrected using the GCR proton flux measured simultaneously by MSL/RAD. The result is a 9-year data set of albedo proton measurements spanning 6 May 2016 to 3 April 2025, which is assumed to depend solely on the near-surface water content of the Martian soil. By correlating MSL/RAD measurements with data from the DAN instrument, also onboard MSL, we show that changes of 2%–7% in soil water content cannot yet be resolved significantly using albedo protons.

However, supporting model calculations suggest that under ideal measurement conditions, MSL/RAD could detect increases in water content of 20% after approximately two to 3 months. Although this required measurement time may seem long, it remains feasible for extended missions like MSL. Variations of 40% in soil WEH content, as may occur near equatorial locations, could be resolved at the 3σ level within roughly 20 days. Poleward, large water reservoirs of 60% and 80% could be detected in about 9 and 5 days, respectively. Since MSL/RAD was not originally designed to measure albedo protons, we additionally considered the expected measurement times for a conceptual detector with a geometry factor of 0.9 cm^{2}sr and a sensitivity range of 20–200 MeV. Such a detector could detect changes in near-surface water content of 20% and 40% after approximately 6–16 and 2 days, respectively. Both scenarios can occur locally, for example, in the Medusae

Fossae Formation, Arabia Terra, or Arcadia Planitia, and therefore represent realistic cases that could be traversed by a future rover or rotorcraft. Even larger variations of 60% and 80% in soil WEH content could be detected almost instantaneously, in less than a day, with statistical significance.

Even though the modeled measurement times for both MSL/RAD and the conceptual detector should be considered conservative lower limits, they nonetheless demonstrate the potential of investigating near-surface water using albedo protons. We therefore propose including albedo proton measurements in future missions to Mars or other extraterrestrial bodies, as they represent a promising complement to existing methods for probing water in soil.

Conflict of Interest

The authors declare no conflicts of interest relevant to this study.

Availability Statement

The data used in this study are archived in the NASA Planetary Data System's Planetary Plasma Interactions Node at the University of California, Los Angeles. The archival volume includes the full binary raw data files, detailed descriptions of the structures, and higher-level data products in human-readable form. The binary MSL/RAD EDR data are archived under (Peterson et al., 2013), while the human-readable MSL/RAD RDR data are archived under (S. Rafkin et al., 2013). The data used to produce the figures in the study are available as open access in Zenodo (Löwe, 2026). More information about the structure of the files will be contained within the files themselves. Additionally, the simulated response matrices for different water contents have been uploaded for further use, for example, with alternative input spectra. The MSL/DAN data set used here includes the published data from Nikiforov et al. (2024) and additional, more recent measurements provided directly by the MSL/DAN team.

Acknowledgments
MSL/RAD is supported by NASA (HEOMD) under Jet Propulsion Laboratory (JPL) subcontract 1273039 to Southwest Research Institute and in Germany by the German Aerospace Center (DLR) and DLR's Space Administration Grant 50QM1701 to the Christian Albrechts-Universität zu Kiel. JLL thanks the MSL/DAN team for their cooperation and for the trust in providing data prior to publication. JLL also would like to thank the reviewers for their efforts in evaluating this work and their helpful comments, which improved the manuscript. SN acknowledges that this material is based upon work supported by Tamkeen under the NYU Abu Dhabi Research Institute Grant CASS. JG thanks the support from the National Natural Science Foundation of China (Grant 42521007). Open Access funding enabled and organized by Projekt DEAL.

References

Abbey, W., Anderson, R., Beegle, L., Hurowitz, J., Williford, K., Peters, G., et al. (2019). A look back: The drilling campaign of the curiosity rover during the Mars science laboratory's prime mission. *Icarus*, *319*, 1–13. https://doi.org/10.1016/j.icarus.2018.09.004

Agostinelli, S., Allison, J., Amako, K., Apostolakis, J., Araujo, H., Arce, P., et al. (2003). GEANT4: A simulation toolkit. *Nuclear Instruments and Methods*, *A506*(3), 250–303. https://doi.org/10.1016/S0168-9002(03)01368-8

Alexander, M. (2001). *Mars transportation environment definition document*. National Aeronautics and Space Administration, Marshall Space Flight Center.

Allison, J., Amako, K., Apostolakis, J., Araujo, H., Arce Dubois, P., Asai, M., et al. (2006). GEANT4 developments and applications. *IEEE Transactions on Nuclear Science*, *53*(1), 270–278. https://doi.org/10.1109/TNS.2006.869826

Allison, J., Amako, K., Apostolakis, J., Arce, P., Asai, M., Aso, T., et al. (2016). Recent developments in GEANT4. *Nuclear Instruments and Methods*, *A 835*, 186–225. https://doi.org/10.1016/j.nima.2016.06.125

Amiri, H. E. S., Brain, D., Sharaf, O., Withnell, P., McGrath, M., Alloghani, M., et al. (2022). The emirates Mars mission. *Space Science Reviews*, *218*(1), 4. https://doi.org/10.1007/s11214-021-00868-x

Anderson, D. M., & Tice, A. R. (1979). The analysis of water in the Martian regolith. *Journal of Molecular Evolution*, *14*(1), 33–38. https://doi.org/10.1007/BF01732365

Appel, J. K., Köhler, J., Guo, J., Ehresmann, B., Zeitlin, C., Matthiä, D., et al. (2018). Detecting upward directed charged particle fluxes in the Mars science laboratory radiation assessment detector. *Earth and Space Science*, *5*(1), 2–18. https://doi.org/10.1002/2016EA000240

Armstrong, R. A. (2022). Forms resembling sponges or corals at gale crater, Mars: Evidence of fossilised life or mineralogy. *Journal of Astrobiology*, *13*, 4–12.

Atri, D., Kamenetskiy, M., May, M., Kalra, A., Castelblanco, A., & Quiñones-Camacho, A. (2025). Estimating the potential of ionizing radiation-induced radiolysis for microbial metabolism on terrestrial planets and satellites with rarefied atmospheres. *International Journal of Astrobiology*, *24*, e9. https://doi.org/10.1017/S1473550425100025

Baade, W., & Zwicky, F. (1934). Cosmic rays from super-novae. *Proceedings of the National Academy of Sciences*, *20*(5), 259–263. https://doi.org/10.1073/pnas.20.5.259

Bartels, J. (1934). Twenty-seven day recurrences in terrestrial-magnetic and solar activity, 1923–1933. *Terrestrial Magnetism and Atmospheric Electricity*, *39*(3), 201–202a. https://doi.org/10.1029/TE039i003p00201

Baydas, S., & Karakas, B. (2019). Defining a curve as a Bezier curve. *Journal of Taibah University for Science*, *13*(1), 522–528. https://doi.org/10.1080/16583655.2019.1601913

Bethe, H. (1930). Zur theorie des durchgangs schneller korpuskularstrahlen durch materie. *Annalen der Physik*, *397*(3), 325–400. https://doi.org/10.1002/andp.19303970303

Boggs, P. T., & Rogers, J. E. (1990). Orthogonal distance regression (Tech. Rep. No. NISTIR 89-4197). *National Institute of Standards and Technology*. Retrieved from https://www.mechanicalkern.com/static/odr_ams.pdf

Boynton, W. V., Feldman, W. C., Mitrofanov, I. G., Evans, L. G., Reedy, R. C., Squyres, S. W., et al. (2004). The mars odyssey gamma-ray spectrometer instrument suite. *Space Science Reviews*, *110*(1), 37–83. https://doi.org/10.1023/B:SPAC.0000021007.76126.15

Boynton, W. V., Feldman, W. C., Squyres, S. W., Prettyman, T. H., Brückner, J., Evans, L. G., et al. (2002). Distribution of hydrogen in the near surface of Mars: Evidence for subsurface ice deposits. *Science*, *297*(5578), 81–85. https://doi.org/10.1126/science.1073722

Butt, Y. M., Torres, D. F., Romero, G. E., Dame, T. M., & Combi, J. A. (2002). Supernova-remnant origin of cosmic rays? *Nature*, *418*(6897), 499. https://doi.org/10.1038/418499a

Cane, H. V. (2000). Coronal mass ejections and Forbush decreases. *Space Science Reviews*, *93*(1–2), 55–77. https://doi.org/10.1023/A:1026532125747

Carr, M. H. (1986). Mars: A water-rich planet? *Icarus*, *68*(2), 187–216. https://doi.org/10.1016/0019-1035(86)90019-9

Carr, M. H., & Head, J. W., III. (2003). Oceans on Mars: An assessment of the observational evidence and possible fate. *Journal of Geophysical Research*, *108*(E5). https://doi.org/10.1029/2002JE001963

Chaffin, M. S., Kass, D. M., Aoki, S., Fedorova, A. A., Deighan, J., Connour, K., et al. (2021). Martian water loss to space enhanced by regional dust storms. *Nature Astronomy*, *5*(10), 1036–1042. https://doi.org/10.1038/s41550-021-01425-w

Christensen, P. R., Jakosky, B. M., Kieffer, H. H., Malin, M. C., McSween Jr, H. Y., Nealson, K., et al. (2004). The thermal emission imaging system (themis) for the mars 2001 odyssey mission. *Space Science Reviews*, *110*(1), 85–130.

Czarnecki, S., Hardgrove, C., Arvidson, R. E., Hughes, M. N., Schmidt, M. E., Henley, T., et al. (2023). Hydration of a clay-rich unit on mars, comparison of orbital data to rover data. *Journal of Geophysical Research: Planets*, *128*(1), e2021JE007104. https://doi.org/10.1029/2021JE007104

Dartnell, L. R., Desorgher, L., Ward, J. M., & Coates, A. J. (2007). Modelling the surface and subsurface Martian radiation environment: Implications for astrobiology. *Geophysical Research Letters*, *34*(2). https://doi.org/10.1029/2006GL027494

Di Achille, G., & Hynek, B. M. (2010). Ancient ocean on Mars supported by global distribution of deltas and valleys. *Nature Geoscience*, *3*(7), 459–463. https://doi.org/10.1038/ngeo891

Dibb, S. D., Hardgrove, C., Lightholder, J., Heffern, L., & Ehresmann, B. (2024). Observed correlation between local topography and passive neutron measurements from the dynamic albedo of neutrons (dan) instrument on the mars science laboratory (msl) rover. *Earth and Space Science*, *11*(10), e2023EA003130. https://doi.org/10.1029/2023EA003130

Donahue, T. M. (1995). Evolution of water reservoirs on Mars from d/h ratios in the atmosphere and crust. *Nature*, *374*(6521), 432–434. https://doi.org/10.1038/374432a0

Drake, D. M., Feldman, W. C., & Jakosky, B. M. (1988). Martian neutron leakage spectra. *Journal of Geophysical Research*, *93*(B6), 6353–6368. https://doi.org/10.1029/JB093iB06p06353

Efron, B., & Tibshirani, R. J. (1994). *An introduction to the bootstrap* (1st ed.). Chapman and Hall/CRC. https://doi.org/10.1201/9780429246593

Ehresmann, B., Zeitlin, C., Hassler, D. M., Wimmer-Schweingruber, R. F., Böhm, E., Böttcher, S., et al. (2014). Charged particle spectra obtained with the Mars science laboratory radiation assessment detector (msl/rad) on the surface of Mars. *Journal of Geophysical Research: Planets*, *119*(3), 468–479. https://doi.org/10.1002/2013JE004547

Engelmann, J. J., Ferrando, P., Soutoul, A., Goret, P., Juliusson, E., Koch-Miramond, L., et al. (1990). Charge composition and energy spectra of cosmic-ray nuclei for elements from be to Ni - Results from HEAO-3-C2 (Vol. *233*, pp. 96–111).

Feldman, W. C., Boynton, W. V., Tokar, R. L., Prettyman, T. H., Gasnault, O., Squyres, S. W., et al. (2002). Global distribution of neutrons from Mars: Results from Mars odyssey. *Science*, *297*(5578), 75–78. https://doi.org/10.1126/science.1073541

Feldman, W. C., Prettyman, T. H., Maurice, S., Plaut, J. J., Bish, D. L., Vaniman, D. T., et al. (2004). Global distribution of near-surface hydrogen on Mars. *Journal of Geophysical Research*, *109*(E9). https://doi.org/10.1029/2003JE002160

Foley, C. N., Economou, T., & Clayton, R. N. (2003). Final chemical results from the Mars pathfinder alpha proton x-ray spectrometer. *Journal of Geophysical Research*, *108*(E12). https://doi.org/10.1029/2002JE002019

Gellert, R., Campbell, J. L., King, P. L., Leshin, L. A., Lugmair, G. W., Spray, J. G., et al. (2009). The Alpha-Particle-X-Ray-Spectrometer(APXS) for the Mars science laboratory (MSL) rover mission. In *40th annual lunar and planetary science conference* (p. 2364).

Ginzburg, V. L., & Syrovatskii, S. I. (1964). The origin of cosmic rays.

Golombek, M. P., Cook, R. A., Economou, T., Folkner, W. M., Haldemann, A. F. C., Kallemeyn, P. H., et al. (1997). Overview of the Mars pathfinder mission and assessment of landing site predictions. *Science*, *278*(5344), 1743–1748. https://doi.org/10.1126/science.278.5344.1743

Gómez-Elvira, J., Armiens, C., Castañer, L., Domínguez, M., Genzer, M., Gómez, F., et al. (2012). Rems: The environmental sensor suite for the Mars science laboratory rover. *Space Science Reviews*, *170*(1–4), 583–640. https://doi.org/10.1007/s11214-012-9921-1

Gonçalves, P., Arruda, L., & Pinto, M. (2022). Validation of dMEREM, the detailed Mars energetic radiation environment model, with RAD data from the surface of Mars. *Frontiers in Astronomy and Space Sciences*, *9*, 833144. https://doi.org/10.3389/fspas.2022.833144

Goossens, S., Sabaka, T. J., Genova, A., Mazarico, E., Nicholas, J. B., & Neumann, G. A. (2017). Evidence for a low bulk crustal density for Mars from gravity and topography. *Geophysical Research Letters*, *44*(15), 7686–7694. https://doi.org/10.1002/2017GL074172

Grotzinger, J. P., Crisp, J., Vasavada, A. R., Anderson, R. C., Baker, C. J., Barry, R., et al. (2012). Mars science laboratory mission and science investigation. *Space Science Reviews*, *170*(1), 5–56. https://doi.org/10.1007/s11214-012-9892-2

Guo, J., Banjac, S., Röstel, L., Terasa, J. C., Herbst, K., Heber, B., & Wimmer-Schweingruber, R. F. (2019). Implementation and validation of the geant4/atris code to model the radiation environment at Mars. *Journal of Space Weather and Space Climate*, *9*, A2. https://doi.org/10.1051/swsc/2018051

Guo, J., Khaksarighiri, S., Wimmer-Schweingruber, R. F., Hassler, D. M., Ehresmann, B., Zeitlin, C., et al. (2021). Directionality of the Martian surface radiation and derivation of the upward albedo radiation. *Geophysical Research Letters*, *48*(15), e2021GL093912. https://doi.org/10.1029/2021GL093912

Guo, J., Slaba, T. C., Zeitlin, C., Wimmer-Schweingruber, R. F., Badavi, F. F., Böhm, E., et al. (2017). Dependence of the Martian radiation environment on atmospheric depth: Modeling and measurement. *Journal of Geophysical Research: Planets*, *122*(2), 329–341. https://doi.org/10.1002/2016JE005206

Guo, J., Wimmer-Schweingruber, R. F., Grande, M., Lee-Payne, Z. H., & Matthiä, D. (2019). Ready functions for calculating the Martian radiation environment. *Journal of Space Weather and Space Climate*, *9*, A07. https://doi.org/10.1051/swsc/2019004

Guo, J., Zeitlin, C., Wimmer-Schweingruber, R. F., Hassler, D. M., Ehresmann, B., Rafkin, S., et al. (2021). Radiation environment for future human exploration on the surface of Mars: The current understanding based on msl/rad dose measurements. *Astronomy and Astrophysics Review*, *29*(1), 8. https://doi.org/10.1007/s00159-021-00136-5

Guo, J., Zeitlin, C., Wimmer-Schweingruber, R. F., Hassler, D. M., Köhler, J., Ehresmann, B., et al. (2017). Measurements of the neutral particle spectra on Mars by msl/rad from 2015-11-15 to 2016-01-15. *Life Sciences in Space Research*, *14*, 12–17. https://doi.org/10.1016/j.lssr.2017.06.001

Guo, J., Zeitlin, C., Wimmer-Schweingruber, R. F., Rafkin, S., Hassler, D. M., Posner, A., et al. (2015). Modeling the variations of dose rate measured by rad during the first msl Martian year: 2012–2014. *The Astrophysical Journal*, *810*(1), 24. https://doi.org/10.1088/0004-637X/810/1/24

Hall, P. (1992). *The bootstrap and edgeworth expansion* (1st ed.). Springer. https://doi.org/10.1007/978-1-4612-4384-7

Hassler, D. M., Zeitlin, C., Wimmer-Schweingruber, R., Böttcher, S., Martin, C., Andrews, J., et al. (2012). The radiation assessment detector (RAD) investigation. *Space Science Reviews*, *170*(1–4), 503–558. https://doi.org/10.1007/s11214-012-9913-1

Heber, B., & Potgieter, M. (2006). Cosmic rays at high heliolatitudes. *Space Science Reviews*, *127*(1), 117–194. https://doi.org/10.1007/s11214-006-9085-y

Hurowitz, J. A., Tice, M. M., Allwood, A. C., Cable, M. L., Hand, K. P., Murphy, A. E., et al. (2025). Redox-driven mineral and organic associations in Jezero crater, Mars. *Nature*, *645*(8080), 332–340. https://doi.org/10.1038/s41586-025-09413-0

Jakosky, B. M., Brain, D., Chaffin, M., Curry, S., Deighan, J., Grebowsky, J., et al. (2018). Loss of the Martian atmosphere to space: Present-day loss rates determined from maven observations and integrated loss through time. *Icarus*, *315*, 146–157. https://doi.org/10.1016/j.icarus.2018.05.030

Jakosky, B. M., Lin, R. P., Grebowsky, J. M., Luhmann, J. G., Mitchell, D. F., Beutelschies, G., et al. (2015). The Mars atmosphere and volatile evolution (maven) mission. *Space Science Reviews*, *195*(1), 3–48. https://doi.org/10.1007/s11214-015-0139-x

Jakosky, B. M., & Phillips, R. J. (2001). Mars' volatile and climate history. *Nature*, *412*(6843), 237–244. https://doi.org/10.1038/35084184

Jokipii, J. R., & Thomas, B. (1981). Effects of drift on the transport of cosmic rays. IV - Modulation by a wavy interplanetary current sheet. *The Astrophysical Journal*, *243*, 1115–1122. https://doi.org/10.1086/158675

Jun, I., Mitrofanov, I. G., Litvak, M. L., Sanin, A. B., Kim, W., Behar, A., et al. (2013). Neutron background environment measured by the Mars science laboratory's dynamic albedo of neutrons instrument during the first 100 sols. *Journal of Geophysical Research: Planets*, *118*(11), 2400–2412. https://doi.org/10.1002/2013JE004510

Kim, S. W., & Kim, K. J. (2026). Monte carlo simulation of lunar regolith neutron leakage under diverse models for sub-surface water detection. *Advances in Space Research*, *77*(8), 8472–8491. https://doi.org/10.1016/j.asr.2025.10.091

Klein, H. P. (1979). The viking mission and the search for life on Mars. *Reviews of Geophysics*, *17*(7), 1655–1662. https://doi.org/10.1029/RG017i007p01655

Köhler, J., Zeitlin, C., Ehresmann, B., Wimmer-Schweingruber, R. F., Hassler, D. M., Reitz, G., et al. (2014). Measurements of the neutron spectrum on the Martian surface with msl/rad. *Journal of Geophysical Research: Planets*, *119*(3), 594–603. https://doi.org/10.1002/2013JE004539

Lauro, S. E., Pettinelli, E., Caprarelli, G., Guallini, L., Rossi, A. P., Mattei, E., et al. (2021). Multiple subglacial water bodies below the south pole of Mars unveiled by new marsis data. *Nature Astronomy*, *5*(1), 63–70. https://doi.org/10.1038/s41550-020-1200-6

Litvak, M. L., Mitrofanov, I. G., Barmakov, Y. N., Behar, A., Bitulev, A., Bobrovnitsky, Y. I., et al. (2008). The dynamic albedo of neutrons (dan) experiment for NASA's 2009 Mars science laboratory. *Astrobiology*, *8*(3), 605–612. https://doi.org/10.1089/ast.2007.0157

Litvak, M. L., Mitrofanov, I. G., Kozyrev, A. S., Sanin, A. B., Tretyakov, V. I., Boynton, W. V., et al. (2006). Comparison between polar regions of Mars from hend/odyssey data. *Icarus*, *180*(1), 23–37. https://doi.org/10.1016/j.icarus.2005.08.009

Löwe, J. L. (2026). Martian proton albedo as signature of near-surface water [Dataset]. *Zenodo*. https://doi.org/10.5281/zenodo.19844278

Löwe, J. L., Khaksarighiri, S., Wimmer-Schweingruber, R. F., Hassler, D. M., Ehresmann, B., Guo, J., et al. (2025). Nowcasting solar energetic particle events for Mars missions. *Space Weather*, *23*(4), e2025SW004372. https://doi.org/10.1029/2025SW004372

Malakhov, A. V., Mitrofanov, I. G., Golovin, D. V., Litvak, M. L., Sanin, A. B., Djachkova, M. V., & Lukyanov, N. V. (2022). High resolution map of water in the Martian regolith observed by frend neutron telescope onboard exomars tgo. *Journal of Geophysical Research: Planets*, *127*(5), e2022JE007258. https://doi.org/10.1029/2022JE007258

Martinez Sierra, L. M., Jun, I., Ehresmann, B., Zeitlin, C., Guo, J., Litvak, M., et al. (2023). Unfolding the neutron flux spectrum on the surface of Mars using the msl-rad and odyssey-hend data. *Space Weather*, *21*(8), e2022SW003344. https://doi.org/10.1029/2022SW003344

Matthiä, D., & Berger, T. (2017). The radiation environment on the surface of Mars – Numerical calculations of the galactic component with geant4/planetocosmics. *Life Sciences in Space Research*, *14*, 57–63. https://doi.org/10.1016/j.lssr.2017.03.005

McDonald, F. B., & Ludwig, G. H. (1964). Measurement of low-energy primary cosmic-ray protons on imp-1 satellite. *Physical Review Letters*, *13*(26), 783–785. https://doi.org/10.1103/PhysRevLett.13.783

Mellon, M. T., & Jakosky, B. M. (1995). The distribution and behavior of Martian ground ice during past and present epochs. *Journal of Geophysical Research*, *100*(E6), 11781–11799. https://doi.org/10.1029/95je01027

Mellon, M. T., McKay, C. P., & Grant, J. A. (2022). Thermal conductivity of planetary regoliths: The effects of grain-size distribution. *Icarus*, *387*, 115211. https://doi.org/10.1016/j.icarus.2022.115211

Mesick, K. E., Feldman, W. C., Mullin, E. R., & Stonehill, L. C. (2020). New and extended data processing of Mars odyssey neutron spectrometer data. *Icarus*, *335*, 113397. https://doi.org/10.1016/j.icarus.2019.113397

Mewaldt, R. A. (1994). Galactic cosmic ray composition and energy spectra. *Advances in Space Research*, *14*(10), 737–747. https://doi.org/10.1016/0273-1177(94)90536-3

Mitrofanov, I. G., Litvak, M. L., Kozyrev, A. S., Sanin, A. B., Tret'yakov, V. I., Grin'kov, V. Y., et al. (2004). Soil water content on Mars as estimated from neutron measurements by the hend instrument onboard the 2001 Mars odyssey spacecraft. *Solar System Research*, *38*(4), 253–257. https://doi.org/10.1023/b:sols.0000037461.70809.45

Mitrofanov, I. G., Litvak, M. L., Varenikov, A. B., Barmakov, Y. N., Behar, A., Bobrovnitsky, Y. I., et al. (2012). Dynamic albedo of neutrons (dan) experiment onboard NASA's Mars science laboratory. *Space Science Reviews*, *170*(1), 559–582. https://doi.org/10.1007/s11214-012-9924-y

Mitrofanov, I. G., Malakhov, A., Djachkova, M., Golovin, D., Litvak, M., Mokrousov, M., et al. (2022). The evidence for unusually high hydrogen abundances in the central part of Valles marineris on Mars. *Icarus*, *374*, 114805. https://doi.org/10.1016/j.icarus.2021.114805

Morgan, G. A., Putzig, N. E., Perry, M. R., Sizemore, H. G., Bramson, A. M., Petersen, E. I., et al. (2021). Availability of subsurface water-ice resources in the northern mid-latitudes of Mars. *Nature Astronomy*, *5*(3), 230–236. https://doi.org/10.1038/s41550-020-01290-z

Morgan, P., Grott, M., Knapmeyer-Endrun, B., Golombek, M., Delage, P., Lognonné, P., et al. (2018). A pre-landing assessment of regolith properties at the insight landing site. *Space Science Reviews*, *214*(6), 104. https://doi.org/10.1007/s11214-018-0537-y

Nazari-Sharabian, M., Aghababaei, M., Karakouzian, M., & Karami, M. (2020). Water on Mars—A literature review. *Galaxies*, *8*(2), 40. https://doi.org/10.3390/galaxies8020040

Nerozzi, S., & Holt, J. W. (2019). Buried ice and sand caps at the north pole of Mars: Revealing a record of climate change in the cavi unit with sharad. *Geophysical Research Letters*, *46*(13), 7278–7286. https://doi.org/10.1029/2019GL082114

Nikiforov, S., Djachkova, M. V., Gellert, R., Mitrofanov, I. G., Lisov, D. I., Litvak, M. L., et al. (2024). Water and chlorine in the Martian subsurface along the 27 km traverse of NASA's curiosity rover according to dan measurements: 2. Results for distinct geological regions. *Journal of Geophysical Research: Planets*, *129*(4), e2022JE007731. https://doi.org/10.1029/2022JE007731

Nikiforov, S., Mitrofanov, I. G., Litvak, M. L., Lisov, D., Djachkova, M., Jun, I., et al. (2020). Assessment of water content in Martian subsurface along the traverse of the curiosity rover based on passive measurements of the dan instrument. *Icarus*, *346*, 113818. https://doi.org/10.1016/j.icarus.2020.113818

Ojha, L., Nerozzi, S., & Lewis, K. (2019). Compositional constraints on the north polar cap of Mars from gravity and topography. *Geophysical Research Letters*, *46*(15), 8671–8679. https://doi.org/10.1029/2019GL082294

Olsson-Francis, K., Doran, P. T., Ilyin, V., Raulin, F., Rettberg, P., Kminek, G., et al. (2023). The cospar planetary protection policy for robotic missions to Mars: A review of current scientific knowledge and future perspectives. *Life Sciences in Space Research*, *36*, 27–35. https://doi.org/10.1016/j.lssr.2022.12.001

Orosei, R., Lauro, S. E., Pettinelli, E., Cicchetti, A., Coradini, M., Cosciotti, B., et al. (2018). Radar evidence of subglacial liquid water on Mars. *Science*, *361*(6401), 490–493. https://doi.org/10.1126/science.aar7268

Parker, T. J., Saunders, R. S., & Schneeberger, D. M. (1989). Transitional morphology in west deuteronilus mensae, Mars: Implications for modification of the lowland/upland boundary. *Icarus*, *82*(1), 111–145. https://doi.org/10.1016/0019-1035(89)90027-4

Pathare, A. V., Feldman, W. C., Prettyman, T. H., & Maurice, S. (2018). Driven by excess? Climatic implications of new global mapping of near-surface water-equivalent hydrogen on Mars. *Icarus*, *301*, 97–116. https://doi.org/10.1016/j.icarus.2017.09.031

Peterson, J., Rafkin, S., Zeitlin, C., Ehresmann, B., Weigle, E., Jeffers, S., & Hassler, D. M. (2013). MSL Mars radiation assessment detector RDR V1.0, MSL-M-RAD-3-RDR-V1.0. *NASA Planetary Data System*. https://doi.org/10.17189/1519761

Picardi, G., Plaut, J. J., Biccari, D., Bombaci, O., Calabrese, D., Cartacci, M., et al. (2005). Radar soundings of the subsurface of Mars. *Science*, *310*(5756), 1925–1928. https://doi.org/10.1126/science.1122165

Posner, A., Richardson, I. G., & Zeitlin, C. J. (2025). Mars ground level enhancements in the context of the solar energetic particle clock. *Solar Physics*, *300*(8), 102. https://doi.org/10.1007/s11207-025-02482-4

Potgieter, M. S. (2013). Solar modulation of cosmic rays. *Living Reviews in Solar Physics*, *10*(1), 3. https://doi.org/10.12942/lrsp-2013-3

Prettyman, T. H., Hagerty, J. J., Elphic, R. C., Feldman, W. C., Lawrence, D. J., McKinney, G. W., & Vaniman, D. T. (2006). Elemental composition of the lunar surface: Analysis of gamma ray spectroscopy data from lunar prospector. *Journal of Geophysical Research*, *111*(E12). https://doi.org/10.1029/2005JE002656

Rafkin, S., Peterson, J., Zeitlin, C., Ehresmann, B., Weigle, E., & Hassler, D. M. o. (2013). MSL Mars radiation assessment detector EDR V1.0, MSL-M-RAD-2-EDR-V1.0t. *NASA Planetary Data System*. https://doi.org/10.17189/1519760

Rafkin, S. C. R., Zeitlin, C., Ehresmann, B., Hassler, D., Guo, J., Köhler, J., et al. (2014). Diurnal variations of energetic particle radiation at the surface of Mars as observed by the Mars science laboratory radiation assessment detector. *Journal of Geophysical Research: Planets*, *119*(6), 1345–1358. https://doi.org/10.1002/2013je004525

Ramirez, R. M., Craddock, R. A., & Usui, T. (2020). Climate simulations of early Mars with estimated precipitation, runoff, and erosion rates. *Journal of Geophysical Research: Planets*, *125*(3), e2019JE006160. https://doi.org/10.1029/2019JE006160

Riu, L., Carter, J., Poulet, F., Cardesín-Moinelo, A., & Martin, P. (2023). Global surficial water content stored in hydrated silicates at Mars from omega/mex. *Icarus*, *398*, 115537. https://doi.org/10.1016/j.icarus.2023.115537

Röstel, L., Guo, J., Banjac, S., Wimmer-Schweingruber, R. F., & Heber, B. (2020). Subsurface radiation environment of Mars and its implication for shielding protection of future habitats. *Journal of Geophysical Research: Planets*, *125*(3), e2019JE006246. https://doi.org/10.1029/2019JE006246

Rummel, J. D., Beaty, D. W., Jones, M. A., Bakermans, C., Barlow, N. G., Boston, P. J., et al. (2014). *A new analysis of Mars "special regions": Findings of the second mepag special regions science analysis group (Sr-sag2)*. Mary Ann Liebert, Inc.

Scheller, E. L., Ehlmann, B. L., Hu, R., Adams, D. J., & Yung, Y. L. (2021). Long-term drying of Mars by sequestration of ocean-scale volumes of water in the crust. *Science*, *372*(6537), 56–62. https://doi.org/10.1126/science.abc7717

Schwadron, N., Wilson, J. K., Jordan, A., Looper, M., Zeitlin, C., Townsend, L., et al. (2018). Using proton radiation from the moon to search for diurnal variation of regolith hydrogenation. *Planetary and Space Science*, *162*, 113–132. https://doi.org/10.1016/j.pss.2017.09.012

Schwadron, N., Wilson, J. K., Looper, M., Jordan, A., Spence, H., Blake, J., et al. (2016). Signatures of volatiles in the lunar proton albedo. *Icarus*, *273*, 25–35. https://doi.org/10.1016/j.icarus.2015.12.003

Seu, R., Biccari, D., Orosei, R., Lorenzoni, L., Phillips, R., Marinangeli, L., et al. (2004). Sharad: The mro 2005 shallow radar. *Planetary and Space Science*, *52*(1–3), 157–166. https://doi.org/10.1016/j.pss.2003.08.024

Seu, R., Phillips, R. J., Biccari, D., Orosei, R., Masdea, A., Picardi, G., et al. (2007). Sharad sounding radar on the Mars reconnaissance orbiter. *Journal of Geophysical Research*, *112*(E5). https://doi.org/10.1029/2006je002745

Simpson, J. (1983). Elemental and isotopic composition of the galactic cosmic rays. *Annual Review of Nuclear and Particle Science*, *33*(1), 323–382. https://doi.org/10.1146/annurev.ns.33.120183.001543

Smith, P. H., Tamppari, L. K., Arvidson, R. E., Bass, D., Blaney, D., Boynton, W. V., et al. (2009). H_2O at the phoenix landing site. *Science*, *325*(5936), 58–61. https://doi.org/10.1126/science.1172339

Stcherbinine, A., Edwards, C. S., Smith, M. D., Wolff, M. J., Haberle, C., Al Tunaiji, E., et al. (2023). Diurnal and seasonal mapping of Martian ices with emirs. *Geophysical Research Letters*, *50*(12), e2023GL103629. https://doi.org/10.1029/2023GL103629

Steele, L. J., Balme, M. R., & Lewis, S. R. (2017). Regolith-atmosphere exchange of water in Mars' recent past. *Icarus*, *284*, 233–248. https://doi.org/10.1016/j.icarus.2016.11.023

Strauss, R., & Potgieter, M. (2014). Where does the heliospheric modulation of galactic cosmic rays start? *Advances in Space Research*, *53*(7), 1015–1023. https://doi.org/10.1016/j.asr.2014.01.004

Takami, H., Kyutoku, K., & Ioka, K. (2014). High-energy radiation from remnants of neutron star binary mergers. *Physics Reviews D*, *89*(6), 063006. https://doi.org/10.1103/PhysRevD.89.063006

Tate, C. G., Moersch, J., Jun, I., Ming, D. W., Mitrofanov, I. G., Litvak, M., et al. (2015). Water equivalent hydrogen estimates from the first 200 sols of curiosity's traverse (Bradbury landing to Yellowknife bay): Results from the dynamic albedo of neutrons (dan) passive mode experiment. *Icarus*, *262*, 102–123. https://doi.org/10.1016/j.icarus.2015.09.002

Tate, C. G., Moersch, J., Mitrofanov, I. G., Litvak, M., Bellutta, P., Boynton, W. V., et al. (2019). Mars science laboratory dynamic albedo of neutrons passive mode data and results from sols 753 to 1292: Pahrump hills to Naukluft plateau. *Icarus*, *330*, 75–90. https://doi.org/10.1016/j.icarus.2019.04.029

Titus, T. N., Kieffer, H. H., & Christensen, P. R. (2003). Exposed water ice discovered near the south pole of Mars. *Science*, *299*(5609), 1048–1051. https://doi.org/10.1126/science.1080497

Usoskin, I. G. (2023). A history of solar activity over millennia. *Living Reviews in Solar Physics*, *20*(1), 2. https://doi.org/10.1007/s41116-023-00036-z

Villanueva, G., Mumma, M., Novak, R., Käufl, H., Hartogh, P., Encrenaz, T., et al. (2015). Strong water isotopic anomalies in the Martian atmosphere: Probing current and ancient reservoirs. *Science*, *348*(6231), 218–221. https://doi.org/10.1126/science.aaa3630

Vos, E. E., & Potgieter, M. S. (2015). New modeling of galactic proton modulation during the minimum of solar cycle 23/24. *The Astrophysical Journal*, *815*(2), 119. https://doi.org/10.1088/0004-637X/815/2/119

Webster, C. R., Mahaffy, P. R., Flesch, G. J., Niles, P. B., Jones, J. H., Leshin, L. A., et al. (2013). Isotope ratios of h, c, and o in co2 and h2o of the Martian atmosphere. *Science*, *341*(6143), 260–263. https://doi.org/10.1126/science.1237961

Wiebel-Sooth, B., Biermann, P. L., & Meyer, H. (1998). Cosmic rays VII. Individual element spectra: Prediction and data. *Astrophysics*, *330*, 389–398. https://doi.org/10.48550/arXiv.astro-ph/9709253

Wilson, J. K., Eke, V. R., Massey, R. J., Elphic, R. C., Feldman, W. C., Maurice, S., & Teodoro, L. F. (2018). Equatorial locations of water on Mars: Improved resolution maps based on Mars odyssey neutron spectrometer data. *Icarus*, *299*, 148–160. https://doi.org/10.1016/j.icarus.2017.07.028

Wilson, J. K., Spence, H. E., Kasper, J., Golightly, M., Bern Blake, J., Mazur, J. E., et al. (2012). The first cosmic ray albedo proton map of the moon. *Journal of Geophysical Research*, *117*(E12). https://doi.org/10.1029/2011JE003921

Xu, Z., Guo, J., Wimmer-Schweingruber, R. F., Dobynde, M. I., Kühl, P., Khaksarighiri, S., & Zhang, S. (2022). Primary and albedo protons detected by the lunar lander neutron and dosimetry experiment on the lunar farside. *Frontiers in Astronomy and Space Sciences*, *9*, 974946. https://doi.org/10.3389/fspas.2022.974946

Zaman, F., Townsend, L. W., de Wet, W. C., Spence, H. E., Wilson, J. K., Schwadron, N. A., et al. (2021). Composition variations of major lunar elements: Possible impacts on lunar albedo spectra. *Icarus*, *369*, 114629. https://doi.org/10.1016/j.icarus.2021.114629

Zeitlin, C., Hassler, D., Cucinotta, F., Ehresmann, B., Wimmer-Schweingruber, R., Brinza, D., et al. (2013). Measurements of energetic particle radiation in transit to Mars on the Mars science laboratory. *Science*, *340*(6136), 1080–1084. https://doi.org/10.1126/science.1235989

Zeitlin, C., Hassler, D. M., Wimmer-Schweingruber, R. F., Ehresmann, B., Appel, J., Berger, T., et al. (2016). Calibration and characterization of the radiation assessment detector (rad) on curiosity. *Space Science Reviews*, *201*(1), 201–233. https://doi.org/10.1007/s11214-016-0303-y